Chem Soc Rev

REVIEW ARTICLE

View Article Online
View Journal

Check for updates

Cite this: DOI: 10.1039/c8cs00320c

Imaging photogenerated charge carriers on surfaces and interfaces of photocatalysts with surface photovoltage microscopy†

Ruotian Chen,[ab] Fengtao Fan,*[a] Thomas Dittrich*[c] and Can Li *[a]

Understanding photogenerated charge separation on the nano- to micrometer scale is the key to optimizing the photocatalytic solar energy conversion efficiency. In the past few years, spatially resolved surface photovoltage (SPV) techniques have opened up new opportunities to directly image localized charge separation at surfaces or interfaces of photocatalysts and thus provided deep insights into the understanding of photocatalysis. In this review, we reviewed the SPV techniques, in particular Kelvin probe force microscopy (KPFM) based spatially resolved SPV techniques and their applications in charge separation imaging. The SPV principle was explained with regard to charge separation across a space charge region (SCR) in a depletion layer at a semiconductor surface and to diffusion. The center of charge approach, relaxation of SPV signals and measurement of SPV signals including SPV transients with fixed capacitors were described. Then, we highlighted the fundamental principle and development of the spatially resolved SPV technique and its application in photocatalysis. Important progress made by the spatially resolved SPV technique in this group is given, focusing on understanding the nature of charge separation and providing insights into the rational design of highly efficient photocatalytic systems. Finally, we discuss the prospects of further developments of the spatially resolved SPV technique that would help in understanding photocatalysis for solar energy conversion with high temporal resolution and operated under *in operando* conditions.

Received 23rd April 2018

DOI: 10.1039/c8cs00320c

rsc.li/chem-soc-rev

---

[a] *State Key Laboratory of Catalysis, Dalian National Laboratory for Clean Energy, The Collaborative Innovation Centre of Chemistry for Energy Materials (iChEM), Dalian Institute of Chemical Physics, Chinese Academy of Sciences, Zhongshan Road 457, Dalian 116023, China. E-mail: ftfan@dicp.ac.cn, canli@dicp.ac.cn*

[b] *University of Chinese Academy of Sciences, Beijing 100049, China*

[c] *Helmholtz-Zentrum Berlin für Materialien und Energie GmbH, Institut für Silizium-Photovoltaik, Kekuléstr. 5, 12489 Berlin, Germany. E-mail: dittrich@helmholtz-berlin.de*

† Part of the themed issue on ''New catalytic materials for an energy and chemistry transition''.

Ruotian Chen

Ruotian Chen received his Bachelor's degree in Physical Chemistry from the University of Science and Technology of China (USTC) in 2013. He is currently a PhD candidate under the supervision of Prof. Fengtao Fan and Prof. Can Li at the State Key Laboratory of Catalysis (SKLC) and the Dalian National Laboratory for Clean Energy (DNL) at Dalian Institute of Chemical Physics (DICP). His research interests focus on photoelectrical imaging microscopy and spectroscopy and their applications in solar energy conversion.

Fengtao Fan

Fengtao Fan received his PhD degree in Physical Chemistry from Dalian Institute of Chemical Physics in 2010. He was promoted to a full professor in 2015 and has been a visiting professor at the Utrecht University. Currently, he is the group leader in the Solar Energy Research Division and the vice director of State Key Laboratory of Catalysis. His research interests include (1) operando spectroscopy (Correlated Raman spectroscopy, Mass spectrometry and Electrochemistry), (2) photoelectrical imaging spectroscopy (KPFM, SPV imaging microscopy), (3) development of Deep Ocean UV Raman spectrograph.

1. Introduction

Because of its unmatched resource potential, solar energy utilization has been the subject of intense research, development, and deployment efforts that have been accelerated during the last decade.[1] Efforts have been focused on artificial photosynthetic systems that directly produce fuels from sunlight.[2,3] Such technologies offer the potential to provide renewable hydrogen by solar-driven water splitting or to produce hydrocarbons directly from sunlight, water, and CO_2.[4] Photocatalytic water splitting using earth-abundant semiconductors is a potentially scalable and economically feasible technology for converting solar energy into fuel and is branded as a Holy Grail of chemistry.[5,6] However, to date, photocatalytic technologies are still in the proof-of-concept stage and face challenges in improving solar-to-hydrogen energy conversion efficiency in order to make solar hydrogen competitive with fossil fuels on the basis of cost-per-energy.[7,8]

Charge separation and transfer (CST) of photogenerated charge carriers is the key ''energy pump and delivery'' step in determining the overall solar energy conversion efficiency in photocatalysis.[9–11] In this respect, substantial work has been devoted to exploring and designing novel photocatalytic systems benefiting charge separation in order to improve the photocatalytic efficiency.[12,13] Several strategies, including heterojunctions,[14–16] phase junctions,[17,18] nano-architectures,[19,20] crystal-facet engineering[21,22] and co-catalyst loading,[9,23] have been developed and give substantial contributions to highly efficient charge separation and high performance of photocatalytic systems. Despite these efforts, a deep understanding of CST processes in photocatalytic systems is still lacking but becomes crucial for further development of the design of advanced photocatalytic systems and further improvement of the photocatalytic efficiency.[24–27]

In recent years, a broad variety of advanced spectroscopic and/or microscopic tools have demonstrated their potential for improving the understanding of complex CST processes in photocatalysts.[28] For example, transient absorption (TA) and transient reflectance (TR) spectroscopies give information about lifetimes of photogenerated electrons and holes even in surface regions according to the decay of TA/TR signals.[27,29–31] X-ray spectroscopy can show local changes of the chemical state affected by CST of photogenerated charge carriers.[32–34] Optical super-resolution microscopy can map surface reaction sites using fluorescence signals in order to reflect the distribution of photogenerated charge carriers at a single-particle level.[35–37] Scanning ultrafast electron microscopy allows the direct observation of the spatiotemporal behavior of the carrier density after optical excitation by using electron energy-gain signals.[38–40] Scanning probe microscopy (SPM) techniques are able to directly image the electric potential or current for monitoring CST processes.[41–43] The progress in the development of characterization techniques for charge separation significantly enhances the understanding of CST processes in photocatalysts and provides insights into further optimization of the performance of photocatalytic systems.

The surface photovoltage (SPV) technique also belongs to the advanced techniques for studying CST processes in photocatalytic systems.[44–49] In comparison with other techniques, SPV signals are directly related to the separation of photogenerated charge carriers in space including the evolution of surface photogenerated charge carriers. This is because the SPV signal is proportional to the amount of separated photogenerated charge carriers (Q) times the charge separation distance (d): $\mathrm{SPV} = Q \times d$.[50,51] The SPV technique is a contactless technique and thus provides non-destructive monitoring of the surface of photocatalysts.[49,52] Moreover, the sensitivity of the SPV technique is on the scale of nV to mV, corresponding to a very low Q of

---

Thomas Dittrich

Thomas Dittrich received his PhD and habilitation degrees from the Faculty of Physics of the Lomonosov Moscow State University in 1990 and from the Technical University Munich in 2002, respectively. Currently, he is a scientist at the Helmholtz-Center Berlin for Materials and Energy and teaches Materials Concepts for Solar Cells at different universities. His current research interests are related to the investigation of photoactive materials for photovoltaics and photocatalysis by applying surface photovoltage methods as main techniques.

Can Li

Can Li received his PhD degree in Physical Chemistry from Dalian Institute of Chemical Physics in 1989. He was promoted to a full professor in 1993 and has been a visiting professor at the Université Pierre et Marie Curie (Paris VI), Lehigh University, the University of Liverpool, and Queensland University. He did his post-doctoral work at Northwestern University in 1994–1996. Currently, he is the head of the Solar Energy Research Division and the director of the Dalian National Laboratory for Clean Energy (DNL). His research interests include (1) UV Raman spectroscopy and time-resolved spectroscopy, (2) environmental and green catalysis, (3) chiral catalysis and bio-catalysis, and (4) solar energy utilization based on photo(electro)catalysis and photovoltaic cells.

about 10^6–10^9 cm^{-2} and a d on the nanoscale. The high sensitivity of the SPV technique enables it to probe a variety of CST processes in complex photocatalytic systems such as drift,[53,54] diffusion,[50,55] trapping[56,57] and polarization.[58,59] The SPV technique also favors a huge time range and a large spectral range and gives rise to the terms 'transient surface photovoltage' (TPV) and 'surface photovoltage spectroscopy' (SPS), respectively.[60,61] These advantages make it possible to distinguish complex CST processes due to variations in time and wavelength for different CST processes.[48,62–64] With the help of the SPV technique, complicated CST processes at the nanoscale have been revealed in many photocatalytic systems and have been well-correlated with the photocatalytic activity.[63,65–70]

Despite great contributions of the SPV technique to the understanding of CST processes in photocatalysts, the conventional SPV technique, which averages SPV signals over a large area, gives only average information about charge separation in photocatalytic particles and aggregations of numerous photocatalytic particles and interfaces. Within individual single photocatalytic particles, even for simple model systems, morphologic, structural and compositional differences clearly exist and lead to an anisotropy of CST processes, which strongly affects the overall performance of photocatalyts.[36] Within a photocatalyst aggregation process, interparticle heterogeneities complicate the matters further.[42] Ensemble-averaged measurements of conventional SPV cannot capture related differences, hampering a deep and clear understanding of complex CST processes. To address this issue, it is significantly important to directly image SPV signals at single photocatalytic particles or interfaces. Now, spatially resolved SPV techniques have opened up new vistas that allow a visualization of localized charge separation and photogenerated charge distributions at surfaces or interfaces of photocatalysts.

In this review, we focus on the use of SPV techniques, in particular spatially resolved SPV techniques, to study or directly image the charge separation and transfer in photocatalytic systems. Firstly, we describe the basic principles of SPV techniques including transient SPV techniques, the experimental set-up and recent advances in their applications in photocatalysis. Secondly, we highlight the spatially resolved SPV techniques based on Kelvin probe force microscopy (KPFM). This section covers a basic primer of KPFM and spatially resolved SPV spectroscopy/microscopy, the experimental set-up and their powerful ability in direct imaging of photogenerated charge carriers at single photocatalytic particles or interfaces, concentrating on giving deeper insights into the driving forces of charge separation and translating these insights into design and optimization of high-efficient photocatalytic systems. Finally, we will give prospects of further developments and applications of SPV techniques in photocatalysis.

2. SPV principle and several cases

2.1 Some basics of the SPV principle

2.1.1 Concept and history of SPV. When photogenerated charge carriers are separated in space, a photovoltage arises due to some charge transfer and/or redistribution. A photovoltage causing a change in the contact potential difference (CPD) at the surface of a sample is called a surface photovoltage (SPV). The SPV is rigidly defined as the illumination-induced changes in the surface potential.[48] The effect was first reported in 1947 by Nobel Prize laureate Brattain,[71] who observed positive contact potential changes on n-type silicon and germanium surfaces and negative contact potential changes on a p-type silicon surface. Bardeen and Brattain first described the SPV technique in 1953. They characterized the light-induced surface potential variation in Ge samples with a mechanically vibrating reed.[72] A detailed account for the SPV is the existence of a space charge layer at the free surface of a semiconductor. In 1955, Garrett and Brattain published a classic paper, where the surface photovoltaic effect was associated with charge separation and transport in a space charge region (SCR) of a semiconductor in theoretical terms.[73]

2.1.2 Formation of SPV at a semiconductor surface. Fig. 1 schematically shows the production of a positive SPV on the surface of an n-type semiconductor. Majority charge carriers are trapped at surface states thus leading to a density of charge in the vicinity of the surface deviating from its equilibrium value and resulting in a surface SCR. This region is also called a depletion region due to the reduced density of majority charge carriers in comparison to its equilibrium value. For n-type semiconductors, electrons are captured by surface states and an upward band bending is formed. Meanwhile, a built-in electric field is formed in a SCR with direction from the bulk to the surface due to the net negative charge at the surface and net positive charge in the SCR. The surface potential (V_S) thus is lower than the potential in the bulk and a surface potential barrier ($|V_S|$) is formed. The value of V_S is determined

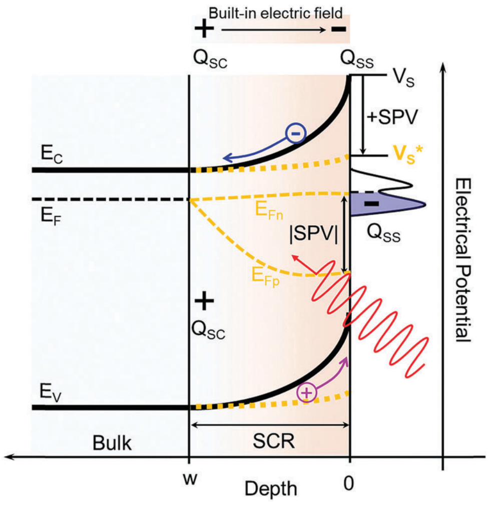

Fig. 1 Schematic band diagram of an n-type semiconductor with a depletion layer (space charge region – SCR) and negative charge trapped at surface states in the dark (black lines) and under illumination (orange lines). E_C, E_V, E_F, E_{Fn}, E_{Fp}, Q_{SC}, Q_{SS}, V_S and V_{S*} denote the conduction and valence band edges, the Fermi energy in thermal equilibrium, the quasi Fermi energies of electrons and holes under illumination, the uncompensated space charge, the charge in surface states and the surface potential in the dark and under illumination, respectively.

by the net surface charge trapped at the surface states. Charge conservation gives:

$$Q_{SS} + Q_{SC} = 0, \tag{1}$$

where Q_{SS} and Q_{SC} are the net areal density of charges at the surface and in the SCR, respectively. A detailed derivation of the dependence of V_S on Q_{SS} can be found in ref. 44. In the depletion regime, the relation can be simplified into:

$$|Q_{SS}| \approx \sqrt{2\varepsilon_S e|N_a - N_d|} \cdot \sqrt{|V_S|}, \tag{2}$$

where ε_S is the dielectric constant of the semiconductor, e is the elementary charge and N_a and N_d are the densities of acceptors and donors respectively. Thus, the surface potential is directly related to the surface charge. Upon illumination, photogenerated electron–hole pairs are separated by the built-in electric field in the SCR. In the SCR of an n-type semiconductor, photogenerated electrons and holes are drifted towards the bulk and surface, respectively, and therefore the net surface charges are reduced. In other words, the surface potential barrier or surface upward band bending is reduced and the surface potential increases. The change of the surface potential results in a SPV. A positive SPV arises under illumination of n-type semiconductors with a depletion layer whereas the SPV corresponds to the reduced degree of band bending or to the splitting potential of quasi-Fermi levels E_{Fn} and E_{Fp}.[74]

In analogy to n-type semiconductors, the SPV is negative for p-type semiconductors.

2.1.3 SPV by charge separation across by a built-in electric field in a SCR. For charge separation in a SCR, the maximum SPV is limited by the surface potential. So, it can be reasonable to apply the saturated SPV in order to measure the band bending ($|V_S|$). Another important parameter is the width of SCR (w), which is given by:

$$w = \sqrt{\frac{2\varepsilon_S|V_S|}{e|N_a - N_d|}}. \tag{3}$$

Photogenerated electron–hole pairs in the SCR can be separated by the built-in electric field, thus yielding the SPV. The SPV can be treated in analogy to the open circuit potential of a solar cell or a photodiode. In the simplest case, the SPV can be expressed by the density of photogenerated charge carriers ($\Delta n = \Delta p$) and the density of minority charge carriers in thermal equilibrium (n_0 or p_0 for p-type or n-type semiconductors, respectively):

$$\mathrm{SPV} = \frac{kT}{e}\ln\left(1 + \frac{\Delta n}{n_0}\right), \tag{4}$$

At low light intensities, the SPV is limited by the shunt resistance and therefore proportional to the photocurrent or Δn so that expression (4) can be written as:

$$\mathrm{SPV} = \frac{kT}{e}\cdot\frac{\Delta n}{n_0}. \tag{5}$$

At high light intensities, Δn is limited by high recombination rates and thus the SPV gets saturated.

In photocatalysis, the built-in electric field in a SCR is a potentially driving force for charge separation.[75,76] Engineering built-in electric fields of photocatalysts by fabricating heterojunctions or crystal facets has been of great interest to improve the charge separation and photocatalytic efficiency.[14,15,22,77] The investigation of SPV on a photocatalyst can give direct information about the concentration and the type of photogenerated charge carriers being separated in built-in electric fields. Besides, the strength of the built-in electric field, the degree of band bending and the width of the SCR can be calculated. Therefore, SPV measurements are highly desirable for the quantitative understanding of the driving force in photocatalysts.

2.1.4 The center of charge approach. Separation of photogenerated charge carriers in space can be caused by drift,[78,79] diffusion, injection, polarization, desorption and adsorption of molecules, surface chemical reactions, and dissociation of excitons. SPV signals are a superposition of all individual changes of potentials caused by separation of photogenerated carriers in space. In measurements of SPV with planar capacitors, a so-called charge separation length can be introduced, which is the difference between the centers of positive and negative charge. The center of charge approach follows directly from the Poisson equation and can really be very useful for the simulation of SPV signals.[50,80] Fig. 2 shows the schematic of the center of charge approach. The centers of negative ($\langle x_n\rangle$) and positive ($\langle x_p\rangle$) charge are functions of time (t) and are defined as:

$$\langle x_n\rangle(t) = \frac{1}{N_Q(t)}\cdot\int_0^H x\cdot n(x,t)\mathrm{d}x, \tag{6}$$

$$\langle x_p\rangle(t) = \frac{1}{N_Q(t)}\cdot\int_0^H x\cdot p(x,t)\mathrm{d}x, \tag{7}$$

where $N_Q(t)$ denotes the total areal density of positive or negative photogenerated charge carriers and is defined as:

$$N_Q(t) = \int_0^H n(x,t)\mathrm{d}x. \tag{8}$$

The charge separation distance (d) is:

$$d(t) \equiv \langle x_n\rangle(t) - \langle x_p\rangle(t). \tag{9}$$

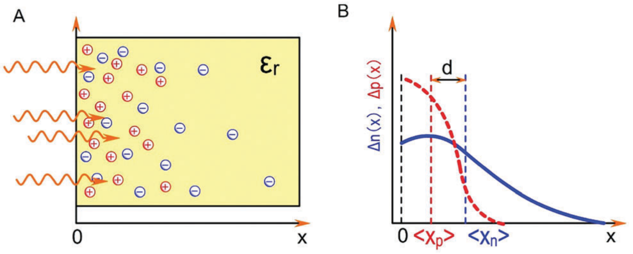

Fig. 2 (A) Schematic of the center of charge approach showing diffusion of electrons and holes in a homogeneous medium. (B) Distributions of photogenerated electrons and holes in depth. The difference between the centers of negative and positive charge is defined as the charge separation length (d).

The SPV signal can be expressed by:

$$\mathrm{SPV}(t) = \frac{e}{\varepsilon_r\varepsilon_0}\int_0^H \mathrm{d}x \int_0^x [n(y,t) - p(y,t)]\mathrm{d}y = \frac{e}{\varepsilon_r\varepsilon_0}\cdot N_Q(t)\cdot d(t). \tag{10}$$

That is, the SPV is split up into two contributions, the total amount of separated charges and the charge separation distance. It is important to remark that the result is valid for any charge separation regime and for any possible time evolution. For the most common regime in photocatalysis, *i.e.* charge separation in a SCR, the value of d is close to the width of the SCR (w) in the low-signal case and can therefore vary between the nanometer and micrometer range depending on doping.

2.1.5 The relaxation of SPV signals. The change of the SPV signals in time after switching off photo-generation is called relaxation of the SPV. The relaxation of SPV signals can be investigated by transient SPV measurements, which give information about carrier dynamics. Typical timescales of different charge separation processes such as drift, diffusion and trapping can be rather different. The relaxation of SPV signals can be limited by processes of recombination or transport. Limitation of relaxation of SPV signals by recombination means that the decay of SPV transients is given by the lifetime of photo-generated charge carriers.[81] This is relevant, for example, for lifetime measurements on conventional semiconductors such as c-Si. Diffusion can influence the relaxation of SPV transients and cause, for example, a local maximum in SPV transients of p-type doped c-Si.[82]

The dielectric or Maxwell relaxation time (τ_M) becomes important for the relaxation of SPV transients on materials with very low conductivity, such as porous or disordered semiconductors.[83] In the case of limitation by τ_M, the SPV signals arise in time due to independent diffusion of photo-generated electrons and holes until the dielectric relaxation time is reached and the SPV signals start to decrease. The value of τ_M can vary over many orders of magnitude, depending on the density and mobility of charge carriers (see Fig. 3).

2.2 SPV measurements

Conventional SPV measurement methods include the SPV measurement with a Kelvin probe and the SPV measurement with a fixed capacitor. Fig. 4A shows the SPV measurement with a conventional Kelvin probe on photocatalysts. The Kelvin probe method enables the direct measurement of the light induced change of the contact potential difference (ΔCPD) and thus a measurement of SPV combined with an illumination system. Recently, the combination of a Kelvin probe with atomic force microscopy (AFM) has evolved into Kelvin probe force microscopy (KPFM) with high spatial resolution, which allows the imaging of SPV up to the nano-meter scale. The basic principle of surface potential measurement with a Kelvin probe and KPFM will be discussed in the next section. Compared with the Kelvin probe method, the fixed capacitor method is important owing to its capability for high resolution in time. In this section, the SPV measurement with a fixed capacitor will be discussed.

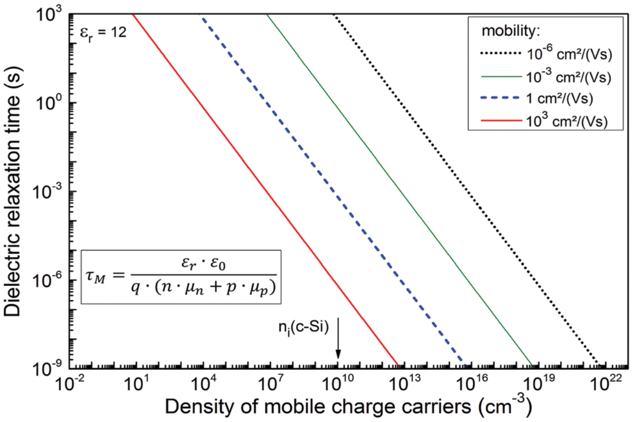

Fig. 3 Dependence of the dielectric relaxation time on the density of mobile charge carriers for mobility values of 10^3 cm^2 V^{-1} s^{-1} (red solid line, characteristic for c-Si), 1 cm^2 V^{-1} s^{-1} (blue dashed line, characteristic of undoped amorphous silicon or TiO$_2$), 10^{-3} cm^2 V^{-1} s^{-1} (green thin line, characteristic of organic semiconductors) and 10^{-6} cm^2 V^{-1} s^{-1} (black dotted line, characteristic of disordered conjugated polymers) in a range between 1 ns and 10^3 s, which corresponds to the range of transient SPV measurements.

Fig. 4B shows the principle of the SPV measurement with a planar capacitor. Planar or parallel plate capacitors can be well applied for the measurement of SPV signals whereas the SPV signals are coupled out with an external measurement capacitor by influence. The measurement capacitor is formed between the sample and reference electrodes. The sample is usually in contact with the sample electrode whereas the reference electrode is connected with the measurement device. A fixed capacitor means that the distance between the sample and reference electrodes is constant. The distance between the sample and reference electrodes can be fixed, for example, with a thin mica sheet. The first measurements of SPV transients with a planar capacitor were shown by Johnson.[81]

Fig. 4C shows the simplified equivalent circuit for transient SPV measurements. Before starting a transient SPV measurement, a zero potential has to be defined at the measurement capacitor. Therefore, the measurement capacitor (capacitance C_m) is shunted by the measurement resistance (R_m). The light pulse for exciting a SPV transient is switched on after the measurement capacitor has been fully discharged.

The measurement capacitor cannot be connected directly with the measurement device due to the mismatch of impedances. For this reason, the reference electrode is connected with a voltage follower or so-called high impedance buffer (order of TΩ) (Fig. 4C).

The resolution time is limited at longer times to the $R_\mathrm{m}C_\mathrm{m}$ time constant and at shorter times to the length of the light pulse and/or to the bandwidth of the high-impedance buffer and of the oscilloscope. SPV transients are usually measured in the 10 ns to 100 ms range. This range is very comfortable for the measurement on many materials. The range of SPV measurements can be extended to the 10^{-9}–10^3 s range by using appropriate light sources and extremely large measurement resistances of hundreds of TΩ.[60]

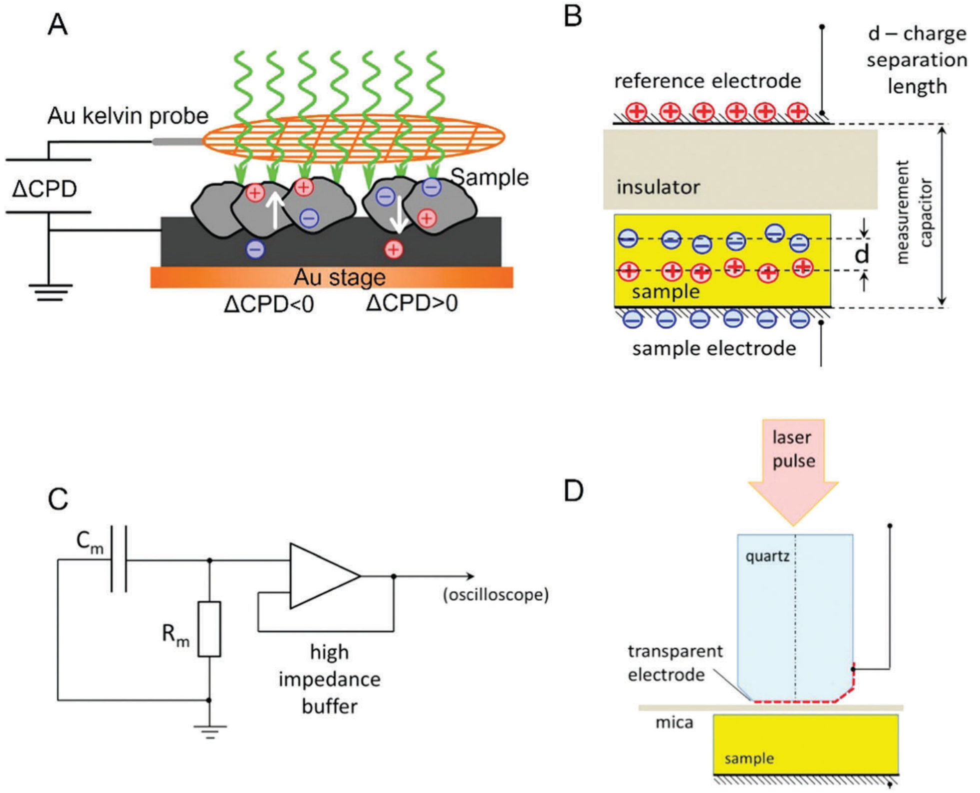

Fig. 4 (A) Principle of the measurement of the light-induced contact potential difference with a (macroscopic) Kelvin probe (vibrating gold mesh) for photocatalytic particles with opposite directions of charge separation. (B) Principle of a SPV measurement with a planar capacitor. (C) Simplified equivalent circuit for transient SPV measurements. (D) Scheme of a suitable electrode configuration in the fixed capacitor arrangement.

SPV measurements in the fixed capacitor arrangement are sensitive in the direction perpendicular to the plates of the measurement capacitor. The sensitivity of transient SPV measurements is of the order of 0.1–1 mV at short times and 10–30 μV at long times and can be further improved by averaging.[84] A logarithmic read-out of SPV transients can be very useful for the measurement of single SPV transients over 6–8 decades in time.[84]

A suitable electrode configuration for transient SPV measurements is shown in Fig. 4D. The transparent electrode can be made from a transparent conductive electrode such as SnO_2:F or a semitransparent metal electrode such as Cr with a thickness of about 15 nm. The electrodes can be deposited onto glass or quartz substrates. For example, an excellently isolating quartz cylinder with a diameter of about 7 mm and a length of about 25 mm can be partially coated with SnO_2:F.

Transient SPV measurements with fixed planar capacitors are complementary to imaging SPV techniques due to the huge time range and high sensitivity which allow, for example, for a relatively high throughput of samples at high resolution in the SPV signals. Furthermore, a large degree of freedom in SPV experiments with fixed capacitors is possible, for example, for measurements in electrolytes, gas atmospheres or vacuum.

2.3 Applications of SPV measurements in photocatalysis

2.3.1 SPV measurements with a Kelvin probe. In this method, the CPD of a photocatalyst film on top of a conductive substrate is typically recorded with a contactless Kelvin probe as a function of the incident photon energy, thus constituting surface photovoltage spectroscopy (SPS).[85] The change of the CPD under illumination corresponds to a photovoltage that develops across the sample film.[86] The sign of the SPV is determined by the type of charge carriers separated towards the surface.[67] The signal of the SPV is limited by the band offsets in the film and provides information about the ability of the photocatalyst to separate charge carriers under illumination. The onset energy of the SPV is usually equal to the effective band gap of the photocatalyst. In this way, SPS provides information about parameters that are central to the operation of photocatalysts.[53]

The key of this method is to identify the dominating charge separation mechanism for a certain photocatalytic system.[52] The identification of the mechanism requires a rational experimental design. A comparison of SPS with absorption spectra is useful to identify the absorption mechanism for the charge separation processes.[65] The investigation of the dependence of SPV on light intensity is also helpful in identifying the charge separation mechanism.[86] The use of electron or hole scavengers and electron or hole blocking layers is also effective at distinguishing between different charge separation processes.[52] For composite photocatalytic systems, a synergistic layer by layer investigation by CPD and SPV is required in order to unravel rather complex charge separation processes.[87,88]

A series of good examples have been reported by Frank E. Osterloh's group, concentrating on understanding the charge separation mechanism of photocatalysts for photocatalytic water splitting.[63,65–67,86] For example, SPV measurements revealed that Ni(0) serves as an electron trap (site for water reduction) and that NiO serves as a hole trap (site for water oxidation) for a NiO_x ($0 < x < 1$) modified $SrTiO_3$ (STO) overall water splitting photocatalytic system. Thus, a three component Ni–STO–NiO_x system with a STO light absorber, a Ni proton reduction and a NiO water oxidation catalyst is devised.[63] SPS studies of Rh-doped $SrTiO_3$ nanocrystals showed that the modification of Ru or Pt cocatalysts and the use of electron or hole scavengers can significantly promote charge separation.[66] The results suggest that charge separation on the nanoscale, where space charge layers are less effective, is strongly influenced by the built-in potential of donor–acceptor configurations, the physical separation of donors and acceptors, and the reversibility of the redox reaction. By comparing the SPV of nano NiO and bulk NiO, it was found that the improved minority carrier extraction in nano NiO contributes to the improved photocatalytic activity for hydrogen evolution from water.[67] These excellent works provide new insight into the charge separation management in photocatalysis.

2.3.2 SPV measurements with fixed capacitors. The fixed capacitor method extends the SPV measurements to modulated SPV and transient SPV.[89] Modulated SPV measurements with fixed capacitors are highly sensitive with respect to charge separation in extremely thin photoactive layers or single nanocrystals.[51,90] For example, a density of charge carriers of only 10^8 cm^{-2} separated in space by 1 nm could be detected.[84] And the method is sensitive to only electronic states and processes that can follow the modulation period in charge separation and relaxation, which favors the direct correlation of SPV with electronically active electronic states and transport processes.[91] Transient SPV measurements would directly reflect the charge carrier dynamics that differ in different charge separation processes.[56] For example, charge separation by the built-in electric field is typically much faster ($<10^{-6}$ s) than carrier diffusion and carrier trapping ($>10^{-5}$).[68,92] Making use of these advantages, the charge separation properties of a wide variety of photocatalytic systems have been revealed.[51,59,68–70,92–97] By combining the modulated and transient SPV measurements, Gross D. *et al.* unambiguously demonstrated the directionality of charge separation in multilayered type II aligned tunneling structures of CdTe and CdSe nanocrystals (Fig. 5A).[51] Fig. 5B shows that the charge separation processes by the built-in electric field and *via* trap states could be separated at different time scales in Fe_3O_4/Fe_2O_3 nanoparticle photocatalysts.[94] Fig. 5C compares the transient SPV of CdS and CdS/WO_3 photocatalysts.[92] A peak of diffusion SPV appears (P_2) after the construction of a CdS/WO_3 nano-junction and gives evidence for the slow recombination rate. Besides, the construction of $BiOI/TiO_2$, Fe_2O_3/TiO_2, ZnO/BiOI, $TiO_2/BiVO_4$ CdSe-QD (quantum dot)/TiO_2 photocatalytic systems has been demonstrated to promote charge separation by applying SPV techniques with fixed capacitors.[68–70,93,98]

However, the detailed analysis of SPV signals is still challenging for related, rather complex, photocatalytic systems (see the schematic in Fig. 6A as an example). Therefore, it is desirable to investigate the behavior of charge separation within single nanocrystals by SPV and to develop adequate models for systems with delocalized and localized electronic states.[99,100]

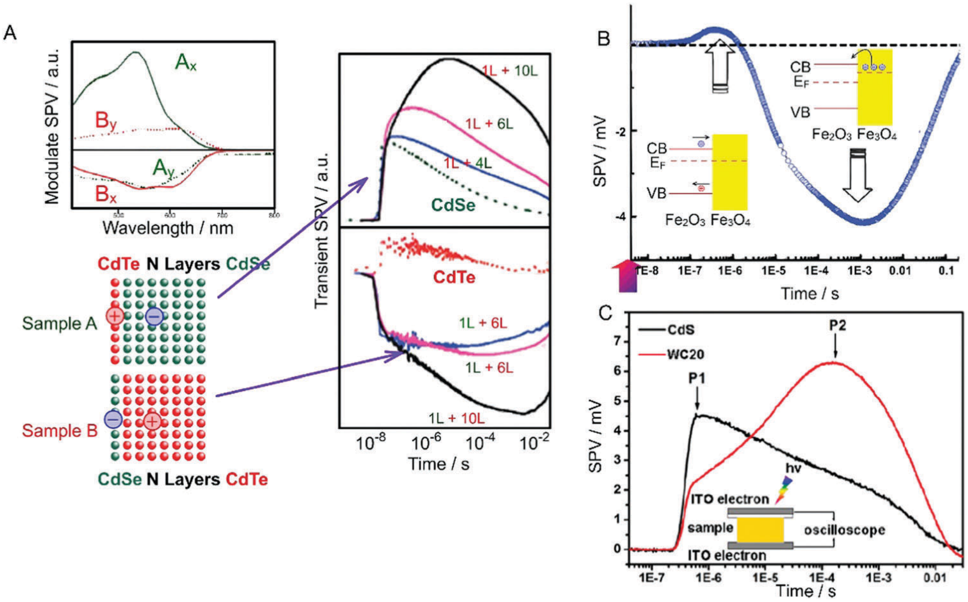

Fig. 5 (A) Modulated SPV spectra and transient SPV of multilayered structures of CdTe/CdSe nanocrystals. Adapted with permission from ref. 51. Copyright 2010, American Chemical Society. (B) Transient SPV of the Fe_3O_4/Fe_2O_3 nanoparticles. Adapted with permission from ref. 94. Copyright 2011, American Chemical Society. (C) Transient SPV of CdS and CdS/WO_3 (WC20) photocatalysts. Reprinted with permission from ref. 92. Copyright 2014, American Chemical Society.

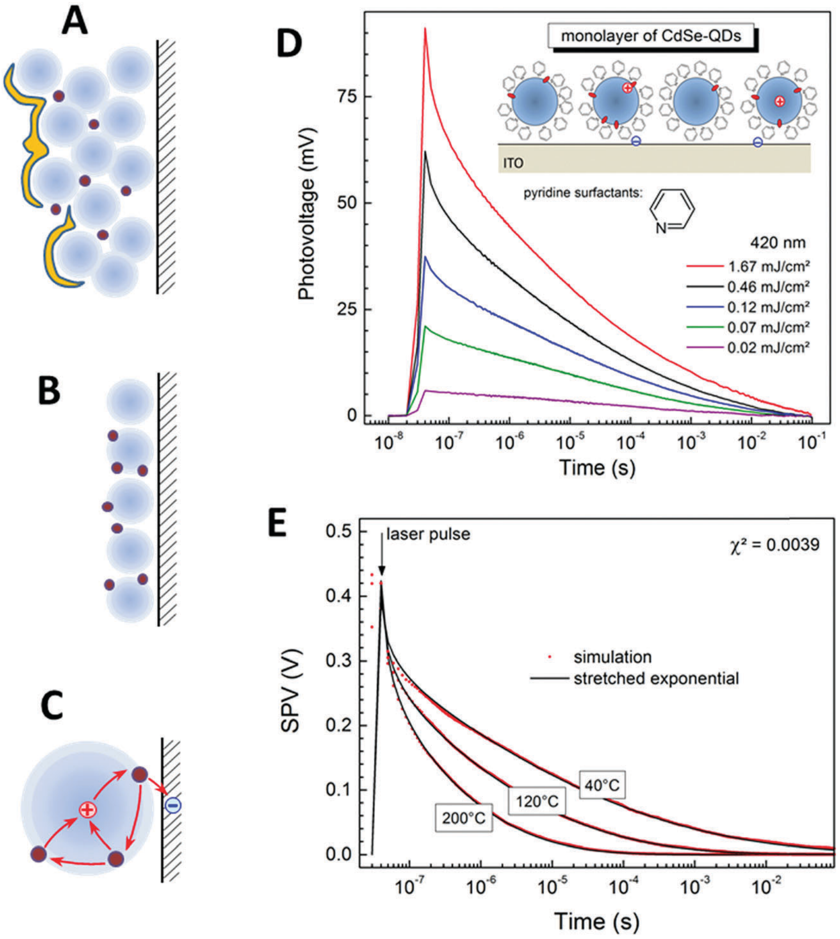

Fig. 6 (A) Schematic of a complex system for SPV experiments with localized and delocalized states. (B) Schematic of a monolayer of QDs as a model system for SPV experiments. (C) Isolated QD with a random walk of a hole in the QD until recombination with the electron which is located at the substrate as an idealized model system for SPV analysis. (D) SPV transients measured on a monolayer of CdSe-QDs (diameter 4.5 nm) covered with pyridine surfactants and deposited onto indium tin oxide. The transients were excited at 420 nm and intensities of 1.67, 0.46, 0.12, 0.07 and 0.02 mJ cm^{-2} (red, black, blue, green and pink lines, respectively). The inset shows a schematic of a monolayer of CdSe-QDs with pyridine surfactants and defect states. For experimental details also see ref. 99. (E) Example for measured SPV transients, which were fitted with stretched exponentials (lines), and for SPV transients simulated and fitted with random walks (circles) for a monolayer of CdSe QDs after ligand exchange with dithiol. Reprinted with permission from ref. 100. Copyright 2013, American Chemical Society.

In this respect, monolayers of QDs (see the schematic in Fig. 6B and C) can serve as excellent photocatalytic model systems[101,102] in order to study charge transport and electronic states in small systems with delocalized and localized states by transient SPV. There are two great advantages of the SPV analysis of a monolayer of QDs. First, in a monolayer of QDs, the QDs can be considered as isolated from each other because charge transfer between neighboring QDs does not change the boundary conditions of the system and can be therefore neglected. Second, it is sufficient to study the transport of only one charge carrier in an isolated QD since only those QDs contribute to the SPV signal from which a charge carrier has been transferred to a substrate and since the probability for photogeneration and charge separation resulting in two or more charge carriers in one QD is extremely low at moderate light intensities.

Fig. 6D shows that the shapes of the SPV transients of a monolayer of CdSe QDs are independent of the intensity of the laser pulse. Therefore, SPV transients of monolayers of QDs can be considered as a superposition of numerous events of charge separation, transport and recombination in an isolated QD (see the schematic in Fig. 6C). Furthermore, the SPV transients occurred within the laser pulse, *i.e.* the initial charge separation was much faster than the resolution time of the experimental set-up. Therefore, SPV transients of monolayers of QDs can be treated as the transfer of charge carriers from numerous QDs to the substrate. Using the transient SPV measurements of monolayers of QDs, the role of ligands of QDs for charge separation could be revealed.[103]

To analyse the SPV transients, random walk simulations have been developed.[56] The distribution and density of localized states at CdSe QDs could be obtained by fitting measured SPV transients with simulated SPV transients by random walks of a hole at an isolated QD recombining finally with an electron, which has been transferred to the substrate during charge separation (Fig. 6E).[100,103] It is also useful to fit a set of measured SPV transients for which one parameter with a strong influence on the measured SPV transients is varied systematically. Such a parameter can be, for example, the temperature (Fig. 6E).[55,61,100] The proposed transient SPV measurements and simulations can be applied to other photocatalytic systems to determine the charge separation, energy distribution and density of localized states.

3. Imaging photogenerated charge on surfaces and interfaces of photocatalysts with spatially resolved surface photovoltage techniques

3.1 A basic primer of spatially resolved SPV techniques in photocatalysis

Since the advent of atomic force microscopy (AFM),[104] a high-resolution technique for topographic mapping of surfaces, the technique has rapidly evolved and is continuously extending its capability, opening new horizons for SPV measurements with high spatial resolution.[105] Kelvin probe force microscopy (KPFM) is an intriguing modified version of AFM that has the capability of simultaneously imaging the surface morphology and surface potential with a spatial resolution on the nanometer scale and an electric resolution of sub-mV.[106] More importantly, the combination of illumination systems with KPFM enables the nanoscale imaging of photo-induced changes of the surface potential, which is the definition of SPV.[48] Recently, therefore, spatially resolved SPV techniques, spatially resolved SPV spectroscopy (SRSPS)[107,108] and SPV microscopy (SPVM)[109–112] or illuminated KPFM, have emerged based on KPFM.[43,113,114] Before discussing spatially resolved SPV, it is essential to briefly explain the fundamentals of KPFM. Next, the basic principle of KPFM to determine the SPV will be discussed. Then, a basic verification of SPVM on photocatalysts will be demonstrated. Finally, we discuss the development of SRSPS in photocatalysts.

3.1.1 Principle of KPFM. As shown in Fig. 7A, when two different materials are brought into electrical contact, the equilibration of the initially different Fermi levels generally leads to charging of the two materials, thus resulting in a potential difference called the contact potential difference (CPD).[115] KPFM maps the CPD between a conducting AFM tip (also called the Kelvin tip) and a sample surface. The CPD between the tip and the sample is defined as:

$$\mathrm{CPD} = \frac{\Phi_\mathrm{t} - \Phi_\mathrm{s}}{e}, \tag{11}$$

where Φ_t and Φ_s are the work functions of the tip and the sample surface.[114,116]

The determination of CPD is based on a Kelvin probe technique, introduced by Lord Kelvin.[117] Fig. 7B shows the energy level diagram of the tip and sample surface when Φ_t and Φ_s are different. Prior to contact, the tip and the sample are electrically neutral and share the same local vacuum level. Upon short-circuiting, the Fermi levels are aligned through charge flow and the system reaches an equilibrium state, as shown in Fig. 7C. The charge flow leads to the charging of the tip and sample surfaces and an electrical force forms in the gap between the tip and sample surface. Meanwhile, the local vacuum levels differ and the corresponding potential difference is known as the CPD. If an applied external bias (V_DC) has the same magnitude as the CPD with opposite direction, the surface charges and the electrical force would be nullified (Fig. 7D). Thus, the CPD is determined by tuning the external bias V_DC to nullify the electrical force. By introducing an AC voltage, the nullification can be easily achieved, as firstly demonstrated by Zisman.[118] Details about the nullification of electrical force are available in ref. 116.

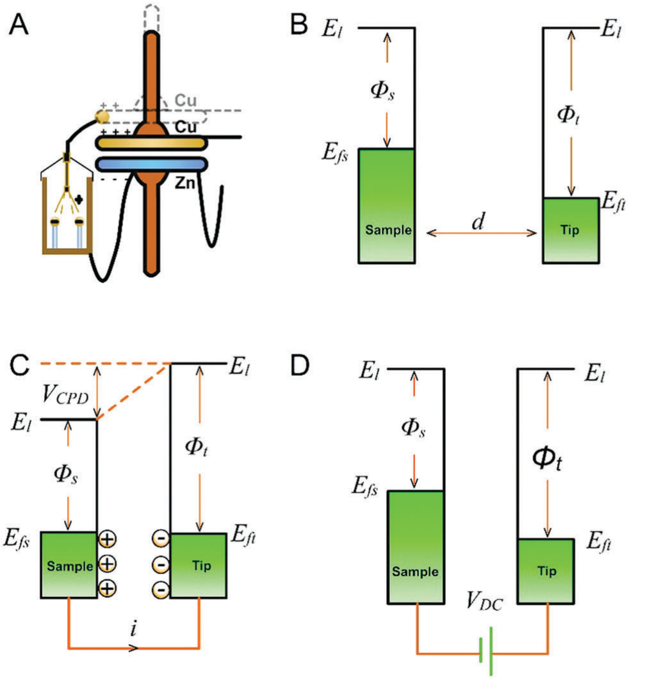

Fig. 7 (A) Schematic showing the charging of two materials with different Fermi levels. (B) Energy level diagram of the tip and sample surface. (C) Alignment of Fermi levels through charge flow. (D) Nullification of surface charges through an applied external bias (V_DC), which has the same magnitude as the CPD with opposite direction. Adapted with permission from ref. 116. Copyright 2011, Elsevier.

3.1.2 Determination of SPV on semiconductor-based photocatalysts by KPFM under illumination. Fig. 8 illustrates the measurement of KPFM on an n-type semiconductor-based single photocatalyst with a surface band bending. Typically, an n-type semiconductor has an upward surface band bending owing to the depletion of majority carriers in a surface region (known as the depletion region or space charge region).[76] The upward band bending leads to a synchronal upward bending of the local vacuum level, resulting in an increase of work function from the bulk to the surface (Fig. 8A). After the operation of KPFM, the local vacuum levels of the sample surface and of the tip are the same. The surface work function is expressed as:

$$\Phi_\mathrm{s} = \Phi_\mathrm{t} - e\mathrm{CPD}. \tag{12}$$

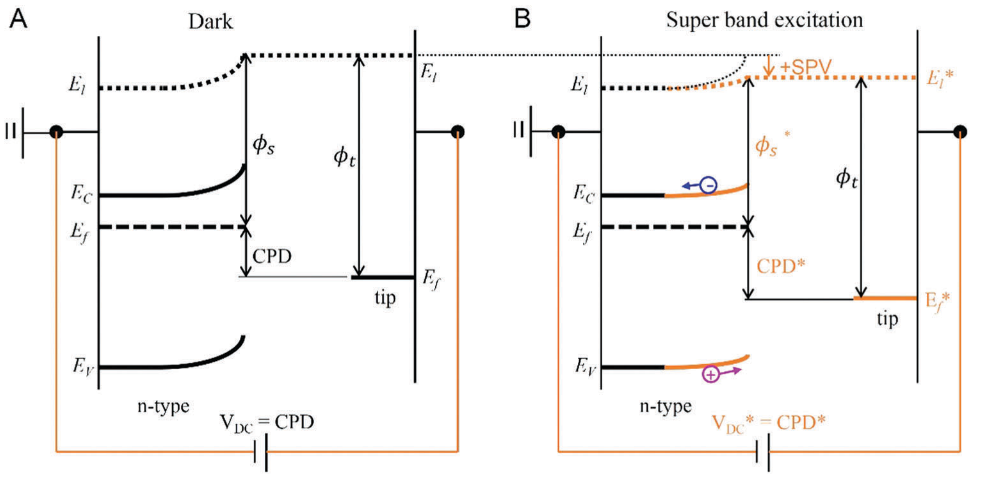

Fig. 8 (A) Measurement of KPFM on an n-type semiconductor-based single photocatalyst with upward surface band bending. (B) Determination of the SPV by KPFM on a single photocatalyst under super-band excitation.

Upon illumination (Fig. 8B), electron–hole pairs are separated in the built-in electric field in the depletion region and the photogenerated holes and electrons are driven towards the surface and the bulk, respectively, leading to a flattened upward surface band bending.[27,76,119,120] In the KPFM measurement, the bulk is grounded and the energy levels of the bulk are unchanged under illumination. Therefore, the flattened upward band bending would decrease the surface work function. The surface work function under illumination is expressed as:

$$\Phi_s{}^* = \Phi_t - e\mathrm{CPD}^*, \quad (13)$$

where Φ_s* and CPD* are the surface work function and the CPD under illumination. Since the work function of the tip does not change under illumination, the SPV can be expressed as:

$$\mathrm{SPV} = \frac{\Phi_s^* - \Phi_s}{-e} = \mathrm{CPD}^* - \mathrm{CPD} = \Delta\mathrm{CPD}. \quad (14)$$

(Note that the surface potential $= \dfrac{\Phi_s}{-e}$ and the SPV is the difference between the surface potentials under illumination and in the dark.) That is, the SPV can be determined by measuring the CPD under illumination and dark conditions. For the n-type semiconductor with upward band bending, as shown in Fig. 8B, the CPD increases under illumination and a positive SPV is yielded. In contrast, for the p-type semiconductor with downward surface band bending, owing to the separation and transfer of photogenerated electrons towards the surface, a decreased CPD and a negative SPV are observed. In this manner, the method of collecting SPV by KPFM on a single photocatalyst has been established.

It should be mentioned that the measurement of SPV is much more complex for composite photocatalytic systems due to the complex charge separation processes on multiple surfaces or at interfaces. Fig. 9A and B schematically show the measurement of CPD and SPV by KPFM on a type II junction photocatalytic system, which is well-developed in photocatalysis.[14,15] The system includes an n-type semiconductor surface and a buried p–n junction interface. The measured SPV can be divided into two contributions, charge separation across the p–n junction (SPV_{p-n}) and charge separation in the surface SCR of the n-type component (SPV_n), $\mathrm{SPV} = \mathrm{SPV}_{p-n} + \mathrm{SPV}_n$ (Fig. 9B). Similar to the single n-type photocatalyst, SPV_n is positive owing to the transfer of holes to the surface, whereas SPV_{p-n} is negative and is supposed to be much larger than the SPV_n, implying that the p–n junction dominates the charge separation process and leads to the transfer of electrons to the surface of the n-type component in the photocatalytic system (negative SPV). As a result, the measurement on the surface of the photocatalysts will yield a negative signal, since $\mathrm{SPV}_{p-n} > \mathrm{SPV}_n$ for most of the cases.

3.1.3 SPV imaging of photocatalysts by SPVM.

By combining the capability of spatial resolution and the determination of SPV, illuminated KPFM shows its potential for direct imaging SPV on photocatalyst particles at nano to micro meter scales. The SPV image is the difference between an illuminated and a dark KPFM scan in the same location. The technique, that can image the SPV, is also called SPVM. Recently, illuminated KPFM has been used to map the spatial heterogeneity of surface photovoltage and to *in situ*/*operando* probe the nano-scale charge transport at interfaces in solar cell materials and devices, giving deep insights for advancing photovoltaics.[109,110,121–124] However, little research has been done on photocatalysts. To verify the reliability of this approach for photocatalysts, we demonstrated the SPV imaging of an n-type and a p-type single photocatalyst by using illuminated KPFM.[125]

n-Type $BiVO_4$ and p-type Cu_2O single crystals are taken as prototypes, which are representative photocatalysts.[126–129] Fig. 10A and B show the KPFM images of a single $BiVO_4$ and Cu_2O particle, respectively. The left half of the KPFM images is mapped in the dark, whereas the right half is mapped under illumination. Upon illumination, we can observe that the KPFM images become brighter for n-type $BiVO_4$, and darker for p-type Cu_2O. The results agree well with the prediction that the CPD increases and decreases for n-type and p-type semiconductors, respectively, verifying the reliability of the illuminated KPFM method

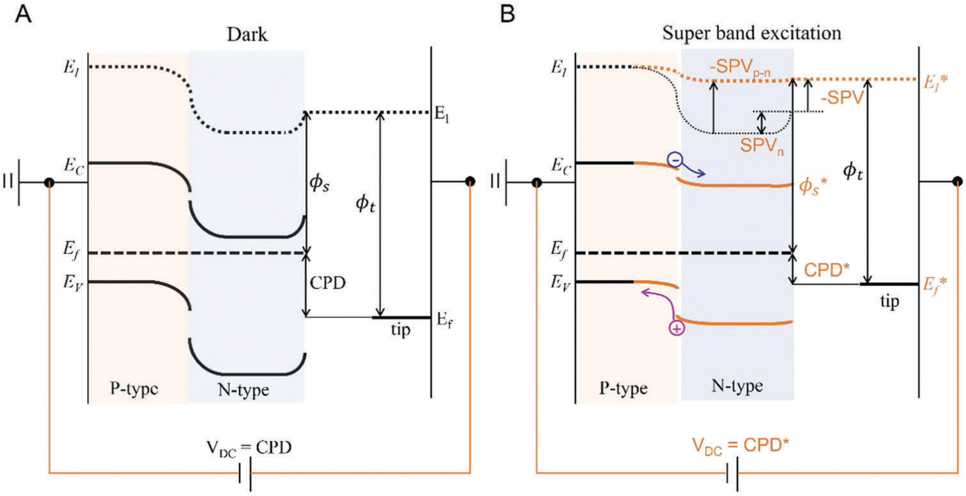

Fig. 9 Schematic showing the measurement of the CPD and SPV by KPFM on a type II junction photocatalytic system in the (A) dark and (B) under super-band excitation.

for SPV imaging of photocatalytic particles.[21,130] Moreover, by extracting the difference of CPD in the dark and under illumination in the same scanning region, we can image the distribution of SPV signals on a single photocatalyst particle. As shown in Fig. 10C and D, the positive SPV and negative SPV distribute on the whole surface of n-type $BiVO_4$ and p-type Cu_2O photocatalysts, respectively. SPV signals are directly related to the photogenerated charge carrier near the surface, *i.e.* the SPV imaging also reflects an image of the distribution of photogenerated charge carriers on the surface. Therefore, one can directly observe that the whole surface of $BiVO_4$ and Cu_2O photocatalysts is dominated by photogenerated holes and electrons, respectively.

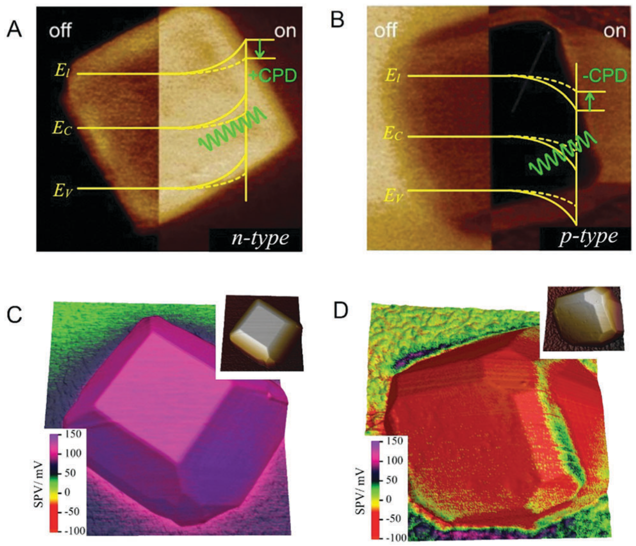

Fig. 10 Predictions of the changes of CPD and KPFM images of a single (A) $BiVO_4$ and (B) Cu_2O particle, respectively. The left half of the KPFM images is mapped in the dark, whereas the right half is mapped under illumination. The SPV image of a (C) $BiVO_4$ and (D) Cu_2O particle, by extracting the difference of CPD in the dark and under illumination. Adapted with permission from ref. 125. Copyright 2017, Royal Society of Chemistry.

In brief, a SPVM image of a photocatalyst is a direct indication of the spatial distribution of photogenerated charge carriers. The region showing positive SPV can be ascribed to the accumulation of photogenerated holes while the region showing negative SPV can be ascribed to the accumulation of photogenerated electrons.

3.1.4 Modulated spatially resolved surface photovoltage spectroscopy (SRSPS). While SPVM can reflect the accumulation of photogenerated charge carriers, modulated SPV was demonstrated to be advantageous for a quantitative understanding of the charge separation process.[43] The modulation can be related to the light intensity, the modulation frequency of the light (time), the voltage bias and the wavelength of modulated light (spectra).[108,111,131,132] The local mechanism of charge separation can be found from the dependence of local SPV signals on the different modulated parameters.

For example, the Ginger group developed intensity-modulated KPFM (IM-KPFM) for probing the charge carrier recombination mechanism in organic solar cells (Fig. 13).[131] IM-KPFM is a frequency-domain measurement that uses the slow response of a standard KPFM feedback loop in order to measure the time-averaged CPD between the tip and sample in response to a modulated illumination source. As the experimental modulation frequency increases, the average CPD will also increase because recombination is too slow to decay completely during a single cycle. The rate at which the average CPD evolves as a function of modulation frequency thus reflects the carrier lifetime (Fig. 11A). Using this method, decay rates of local SPV signals were revealed (Fig. 11B), especially useful for correlating the role of the microstructure with a specific type of recombination mechanism.

The application of the different kinds of modulations is also important for the investigation of photocatalysts. Besides the origination of SPV from charge separation in photocatalysts, the photo-induced CPD changes might also be affected by other factors, such as photo-induced heating, photo-induced changes in the atmosphere, photochemical processes and occupation of

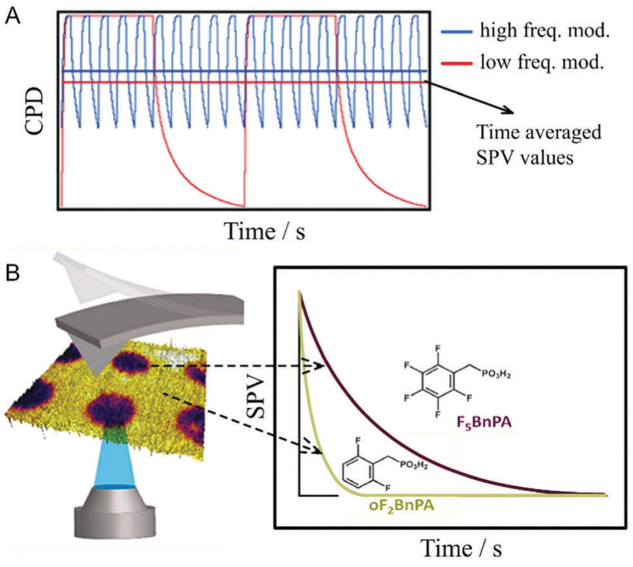

Fig. 11 Intensity-modulated KPFM (IM-KPFM) for probing the recombination mechanism in organic photovoltaics. (A) Oscillations of the surface potential with different light modulation periods. The horizontal lines show the time-averaged values; (B) decay rate of local SPV signals for correlating the role of the different compositions with a specific type of recombination mechanism. Adapted with permission from ref. 131. Copyright 2014, American Chemical Society.

deep defect states.[48] Such factors usually produce very slow or even non-reversible SPV signals,[62,133,134] the time scales of which are from s to h or longer, and contribute only little to photocatalytic reactions at the ms to s time scale.[24,25] Frequency-modulated SPV shall be applied in order to get rid of the influence of very slow processes on the SPV signals. In addition, spectral-dependent SPV, that is SPS, is also useful because very slow processes can induce SPV signals at photoexcitation energies below the band gap of semiconductor photocatalysts.[48] For this reason, frequency-modulated spatially resolved surface photovoltage spectroscopy (SRSPS) based on the modification of illuminated KPFM was developed in this group[108] in order to rule out the influence of slow processes on SPV signals and thus become capable of quantitatively measuring the driving forces of charge separation in relation to photocatalytic reactions.

Fig. 12 compares the measurement of SPS on a $BiVO_4$ single crystal photocatalyst by using illuminated KPFM and SRSPS.[108] For the SPS obtained by illuminated KPFM (Fig. 12A), the onset of SPV is below the band gap (2.4 eV). In contrast, the SPS spectrum measured by the SRSPS technique appeared at 2.4 eV and corresponded to excitation above the band gap, also called super-band SPV (Fig. 12A). The decay of the CPD after switching off illumination provides two processes (Fig. 12B), a slow (minute scale) and a fast (less than one second) one. The slow component disturbs the quantitative analysis of charge separation in relation to the photocatalytic performance. The slow component can be filtered out by the SRSPS technique. This example shows the high performance of SRSPS for achieving a quantitative understanding of charge separation processes in photocatalysts. A detailed description of SRSPS will be given in the next section.

3.2 Experimental set-up

Developing a technique that enables the quantitative understanding of SPV at the nano-meter scale is challenging due to the complexity of SPV signals that are affected by many factors. To quantify the SPV signals at the nano-meter scale, we developed a spatially resolved SPV technique with frequency and wavelength modulation. Fig. 13 shows our experimental set-up. The apparatus includes three essential components: the system for illumination, the KPFM system and the data acquisition system.

A xenon lamp combined with a monochromator is used for wavelength-dependent photoexcitation of SPV signals. After passing through the monochromator, the light is focused on the sample by a set of lenses. A chopper is placed between the lenses to achieve frequency modulation. The light source can be replaced by a laser equipped with neutral density filters to achieve light intensity modulation.

Typically, amplitude-modulated (AM) KPFM is implemented for photocatalysts due to its high energy resolution (5 mV) at

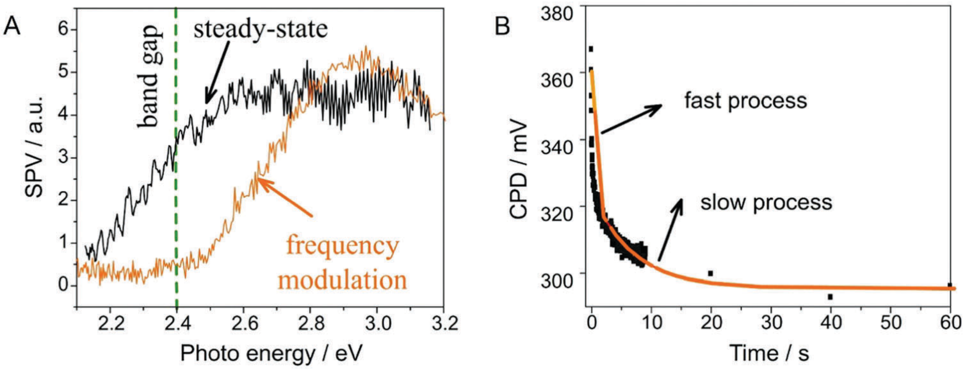

Fig. 12 (A) Measurement of SRSPS on a $BiVO_4$ single crystal photocatalyst using steady-state and frequency-modulated illuminated KPFM. (B) Decay of the CPD after switching off illumination undergoing a slow and a fast process. The slow process can be filtered out by frequency-modulated KPFM and SRSPS. Adapted with permission from ref. 108. Copyright 2015, Wiley-VCH Verlag GmbH & Co.

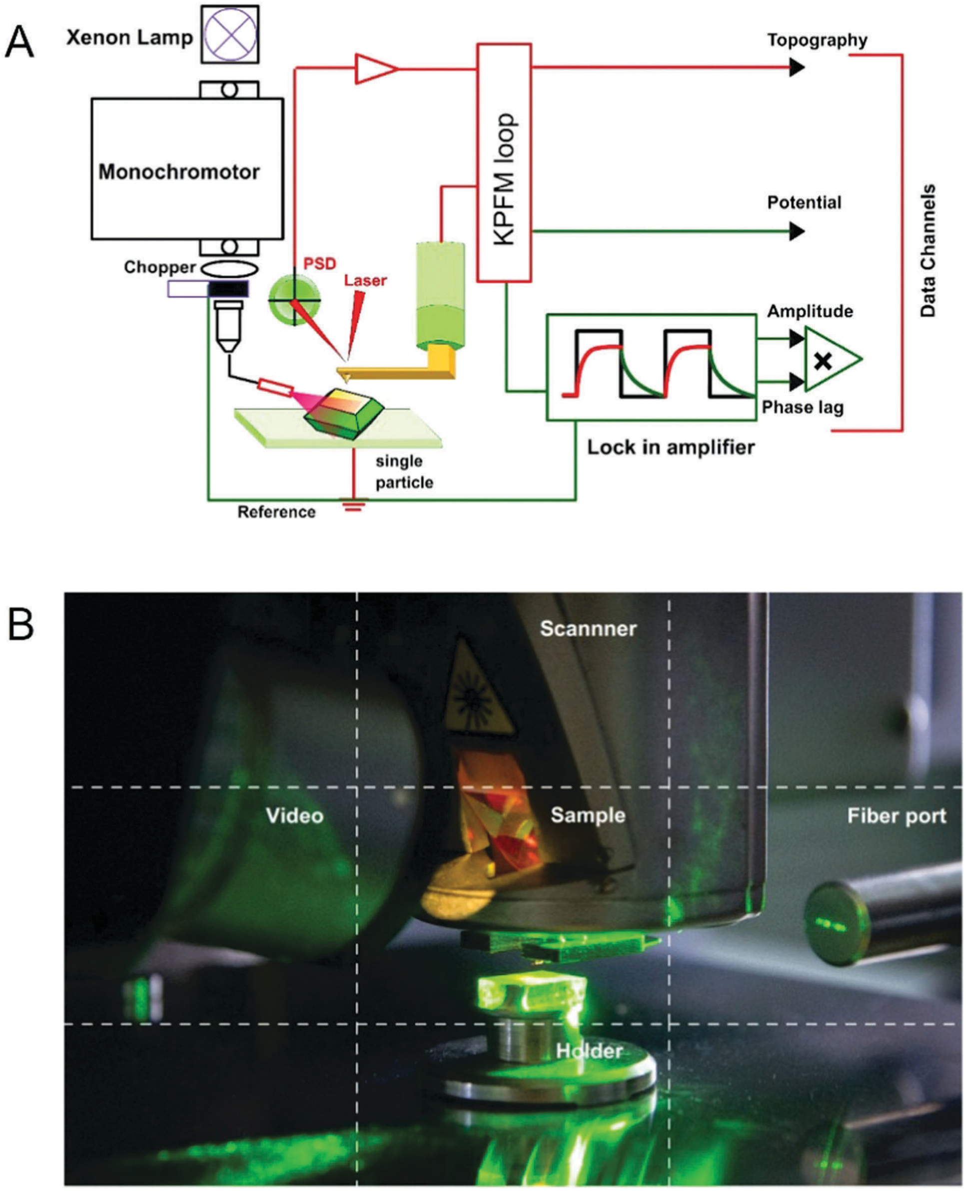

Fig. 13 (A) Schematic diagram of three key components: system for illumination, KPFM system and system for data acquisition for the measurement of spatially resolved SPV and (B) photograph of the local structure of the equipment.

low AC voltage.[116] The low AC voltage (≤ 1 V) is important for the investigation of photocatalysts due to the high-bias induced band bending effect on the semiconductor surface.[135] Commercially available tips for KPFM, for example, Pt/Ir coated Si tips, are commonly used for KPFM imaging with a resolution in the nm range (1–100 nm). For reaching a sub-nanometer spatial resolution, a sharp needle tip and frequency-modulated (FM) KPFM are needed.[136] In AM KPFM mode, for each scan, the probe passes over the surface twice. On the first pass, the topography is acquired in the tapping mode. Then, a second pass is executed along the first pass profile at a lift height of 20–100 nm from the first pass height, recording the CPD signal using a KPFM loop. Thus, a spatial relation between morphology and surface potential distributions can be established.

A steady-state SPV signal is obtained by direct subtraction between a steady-state illuminated and a dark KPFM scan at the same location. To fetch the modulated SPV signal, the varied CPD signals induced by chopped light form output to another external lock-in amplifier and are synchronized with the chopped signals. Incidentally, measurements with lock-in amplifiers are highly sensitive due to the measurement principle with a phase-sensitive rectifier. The variations of CPD signals are obtained in form of the amplitude (R) and the phase (θ) at the output of the lock-in amplifier. The amplitude is directly proportional to the SPV signal, which reflects the amount of photogenerated charge separated in space. The phase is directly related to the sign of the SPV, which reflects the direction of photogenerated charge separation. In our setup, typically, the phase lags between the excitation signal and the obtained

CPD signal are approximately 120° for the measurement of SPV on an n-type photocatalyst surface, corresponding to positive SPV signals.[108] However, the phase lags are approximately −60° for a p-type photocatalyst surface, corresponding to negative SPV. The two phase lags with a phase difference of 180° correspond to two directions of charge separation.[137] A change of the relaxation of SPV signals, for example, due to trapping at deep surface states, would cause a change in the phase.[137] Thus, the phase is also important for distinguishing between different charge separation and relaxation processes. The obtained R and θ values, together with the wavelength of the incident light, constitute the surface photovoltage spectra and surface photovoltage phase spectra, respectively. By fixing the tip on a desirable position, SRSPS, including amplitude SPS and phase SPS, can be obtained.

3.3 Application of spatially resolved SPV techniques in photocatalysis

Photocatalysts have the potential to directly convert solar energy into chemical fuels.[1] To achieve highly-efficient solar to fuel conversion, the photogenerated charges are required to be effectively separated toward the surface of the photocatalysts, at which they are utilized for chemical reactions.[5,36] In the last decade, many strategies have been developed to enhance the photocatalytic efficiency by fabricating the photocatalysts with heterojunctions,[138] phase junctions,[17] co-catalysts,[9] nanosteps,[139] interfaces[140] and crystal facets[21] (Fig. 14). Benefiting from these nm-scale heterostructures, the photogenerated electrons and holes are separated and transferred to spatially-separated surface locations for reduction and oxidation reactions and therefore the photocatalytic performance has been significantly improved. The improvement is generally attributed to the formation of junctions that drive charge separation *via* a built-in electric field.[14,15,20] However, whether the junction or the built-in electric field is available and active in these nanostructures and how it drives charge separation and to what extent are far from being well understood. The lack of understanding of charge separation becomes the bottleneck in further improving the photocatalytic efficiency.

KPFM and SPVM are promising techniques that can directly measure the built-in potential and charge separation at the nm-scale interfaces[122,141] or individual heterostructures.[142–145] Fig. 15A shows a direct imaging of built-in potential distributions at a CdS/PbS p–n junction[143] by KPFM. The potential changes (from 375 mV to 510 mV) on the tens of nanometer scale would form a huge built-in electric field for charge separation (electric field ~10^7 V m^{-1}). Therefore, the measurement of spatial potential distributions thermodynamically evaluates the driving forces of charge separation. Fig. 15B shows a direct spatial charge separation at the Au-nanoparticle/TiO_2-nanotube interfaces with illuminated KPFM.[146] Approximately 0.3 electron per Au particle of about 4 nm in diameter is effectively charged. Thus, the actual spatial charge separation behavior is revealed by the photo-induced surface potential changes (SPV), which can be imaged by illuminated KPFM or SPVM.[111,147,148] These examples well demonstrated the powerful capability of KPFM-based SPV techniques in quantitative understanding of charge separation in nm-scale structures. For actual photocatalytic systems, the quantitative understanding of charge separation can be more difficult due to the multifold charge

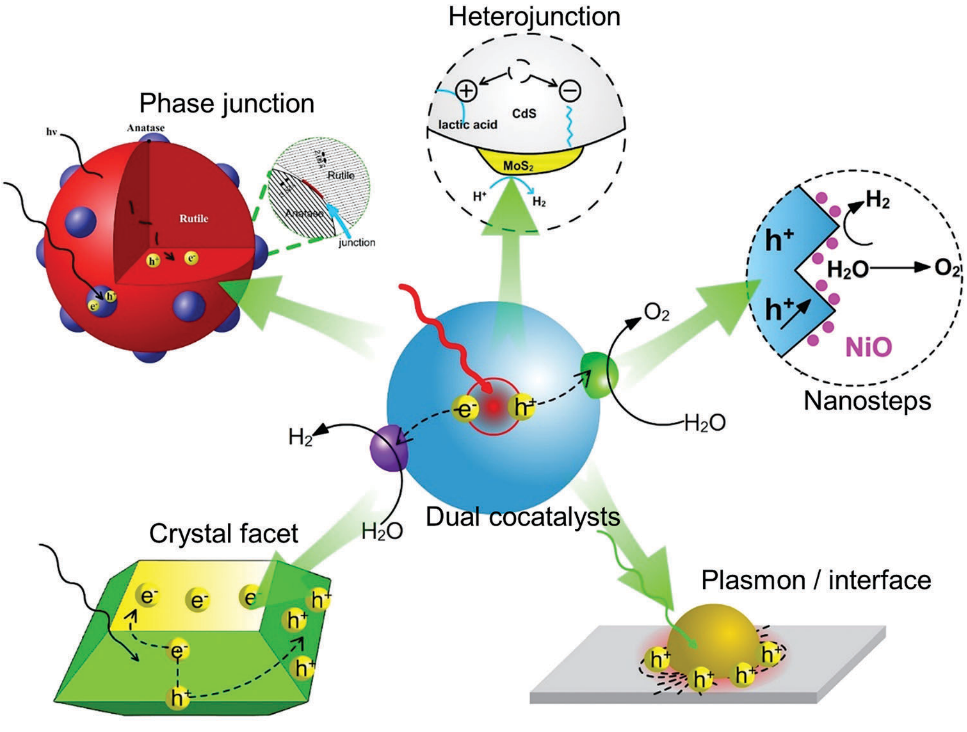

Fig. 14 The developed strategies for fabricating efficient photocatalytic systems.

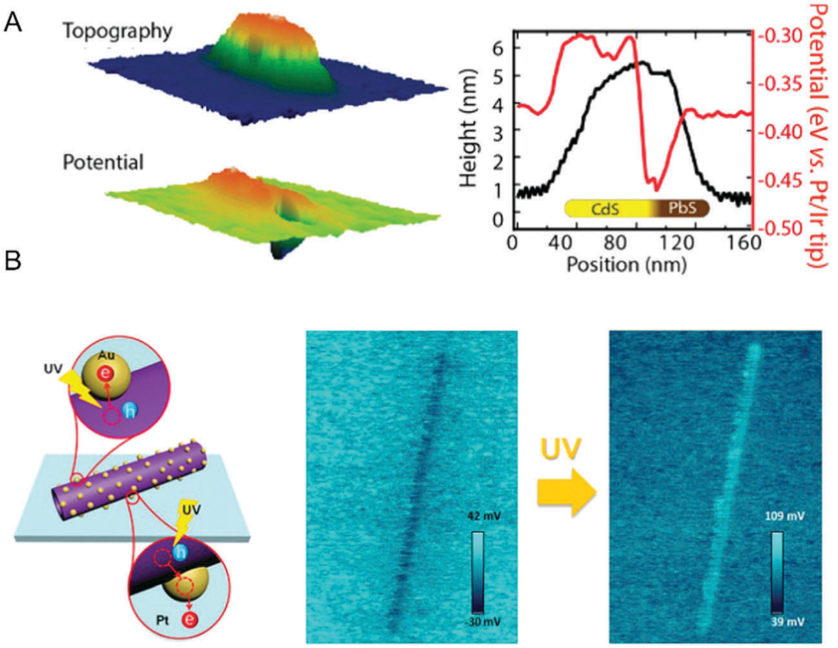

Fig. 15 (A) KPFM study of built-in potential distributions at a CdS/PbS p–n junction. Reprinted with permission from ref. 143. Copyright 2013 American Chemical Society. (B) Photo-excited KPFM study of spatial charge separation at the Au-nanoparticle/TiO_2-nanotube interfaces. (Reprinted with permission from ref. 146. Copyright 2014 American Chemical Society.)

separation processes that are affected by many factors, while can be settled by the modulated SPV approaches (see Section 3.1.4). With these insights, we have developed a modulated, spatially-resolved and KPFM-based SPV technology and applied it to quantitatively understand the built-in electric field and charge separation in actual photocatalytic systems. In the following sections, recent applications of SRSPS and SPVM in combination with KPFM on these photocatalysts are reviewed. These methods, with nanoscale spatial resolution and mV sensitivity, can figure out the existence of the built-in electric fields, visualize charge separation and transfer on the surface or at the interface, quantify the driving forces of charge separation and give deep insights into how to design highly-efficient photocatalysts.

3.3.1 SCR beneath the facets of photocatalyst crystals. Engineering photocatalysts with controlled morphology and preferentially exposed facets has attracted much attention due to spatial heterogeneity in photocatalytic reactions.[149–154] Early in 2002, Matsumura and coworkers reported that photo-reduced Pt particles and photo-oxidized PdO_2 can be formed on different facets of well crystallized rutile and anatase particles.[155] With single-molecule fluorescence spectroscopy, Majima *et al.* showed that probe molecules were selectively reduced by photo-generated electrons and located on facets of single crystals of TiO_2.[156] Similar results were found on monoclinic bismuth vanadate (m-$BiVO_4$) and Cu_2O.[127,157,158] Studies demonstrated that monoclinic bismuth vanadate crystals with preferentially exposed facets exhibit greatly enhanced activity in photocatalytic oxidation of water for O_2 generation.[158,159] KPFM maps the crystal-facet-dependent work function on Cu_2O single crystals.[144] Our previous results demonstrate that the reduction and oxidation cocatalysts can be deposited on the {010} and {110} facets of $BiVO_4$ in a spatially separated way.[21] By using aqueous-phase AFM, Mul *et al.* have shown that photodeposition of Pt nanoparticles on platelets of WO_3 crystals occurs preferentially on the small, subordinate facets with intrinsic surface charge rather than photogenerated charges.[160] More recently, crystal-facet-dependent charge dynamics on single photocatalysts were revealed by single particle spectroelectrochemistry[161] and first-principles simulations.[162]

Despite these efforts in understanding the role of different facets in photocatalysis, the intrinsic reasons and processes are not yet well understood. We reported the revealing of anisotropic photoinduced charge distributions on different facets of $BiVO_4$ single particles by SRSPS.[108] Fig. 16A shows the dark-state surface potential images of a single $BiVO_4$ crystal with exposed {010} and {011} facets. The image clearly shows the diversity of the potential within a single crystal and indicates that the two facets have different SCRs beneath the surfaces, although they share the same bulk Fermi levels. Upon irradiation with modulated light, the overall surface potential of the whole crystal is increased, as shown in Fig. 16B. More importantly, a large number of stripes were observed due to the variation of the surface potential, and are mainly distributed on the {011} facets. The consistency of the 10 Hz frequency of the surface potential variations with that of the chopped light undoubtedly confirms the existence of built-in electric fields and the separation of photogenerated charges on the surface of the crystal. To give a quantitative description of the process, the surface potential signals were fed to a lock-in amplifier, and synchronized with the chopped signals. All the amplitude spectra in Fig. 16C show SPV responses at a photoexcitation

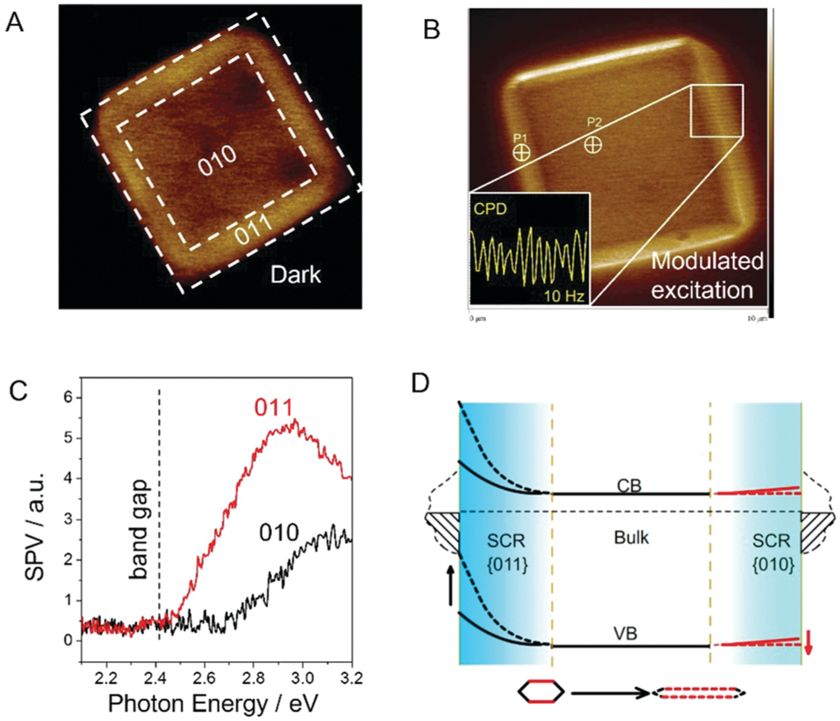

Fig. 16 (A) Dark-state surface potential images of a single $BiVO_4$ crystal with exposed {010} and {011} facets. (B) KPFM image of a single $BiVO_4$ excited with modulated UV light. (C) Representative SRSPS obtained on the {010} and {011} facets. (D) Schematic showing the distribution of SCRs beneath the {010} and {011} facets of a $BiVO_4$ crystal with two morphologies. Adapted with permission from ref. 108. Copyright 2015, Wiley-VCH Verlag GmbH & Co.

energy greater than 2.4 eV, which is super band excitation. The positive theta value of around 120 degree on both facets indicates that the photogenerated holes are drifted to the surface of the crystal due to the existence of built-in electric fields in n-type semiconductors. The amplitude of SPV measured on the {011} facet is much more intensive than that on the {010} facet. Further quantitative studies demonstrated that the difference of SPV amplitude can be increased to 70 times with increased signal on the {010} facet and decreased signal on the {011} facet by tuning the ratio of the {010} facet and the {011} facet, as shown in Fig. 16D. Larger anisotropic charge separation on different facets accounts for higher photocatalytic performance.[159]

The study for the first time proved that different facets of photocatalysts possess different built-in electric fields and can result in anisotropic photoinduced charge transfer. Besides, the result suggests that morphology engineering plays a key role in tuning the distribution of built-in electric fields for enhanced photocatalytic performance (this part of study will be published in a following paper with 2D simulation of the built-in electric field).

3.3.2 Alignment of built-in electric fields by cocatalysts. Photocatalysts based on semiconductor particles together with cocatalysts for oxidation and reduction are key components for the direct conversion of sunlight into fuel.[9] Cocatalysts are absolutely necessary and important for most catalytic systems. A rational assembly of cocatalysts on specific sites of photocatalysts can significantly promote the photocatalytic efficiency.[163] However, the complexity of photocatalysis due to both surface catalysis and charge transfer together with the small size (nm to µm) makes a deeper understanding of the precise role of cocatalysts rather challenging.[23] KPFM and SRSPS with spatial resolution and energy resolution provide an opportunity to study this issue. Here, SPVM and SRSPS were used to understand the role of cocatalysts for high-efficient photocatalytic performance.[164]

$BiVO_4$ single photocatalyst particles with facet-selectively photodeposited MnO_x nanoparticles on the {011} facets were chosen as a model system (Fig. 17A) and were studied by SRSPS. Fig. 17B shows that, after selective deposition of MnO_x cocatalysts on the {011} facets, the SPV signals measured at the {011} facets increased by more than three times. More interestingly, the sign of the SPV signal at the {010} facet changed to negative whereas the absolute values of the SPV signals were increased by more than three times. A subsequent experiment showed that the surface potentials on the {011} facets could be tuned while those of the {010} facets remained the same upon increasing the particle size of nano MnO_x cocatalysts. It is reasonable to suppose, due to different work functions, that an efficient junction was formed between MnO_x nanoparticles and $BiVO_4$ photocatalysts.[165] The transfer of electrons from $BiVO_4$ to MnO_x would result in a decrease of E_F in the bulk of $BiVO_4$ photocatalysts. As a consequence, in the case of the pinning of E_F on the {010} facets, the direction of band bending and of the built in electric field would change beneath the {010} facets whereas the strength of the built in electric field between two facets would strongly increase. A fit of the measured distribution of the surface potential showed that

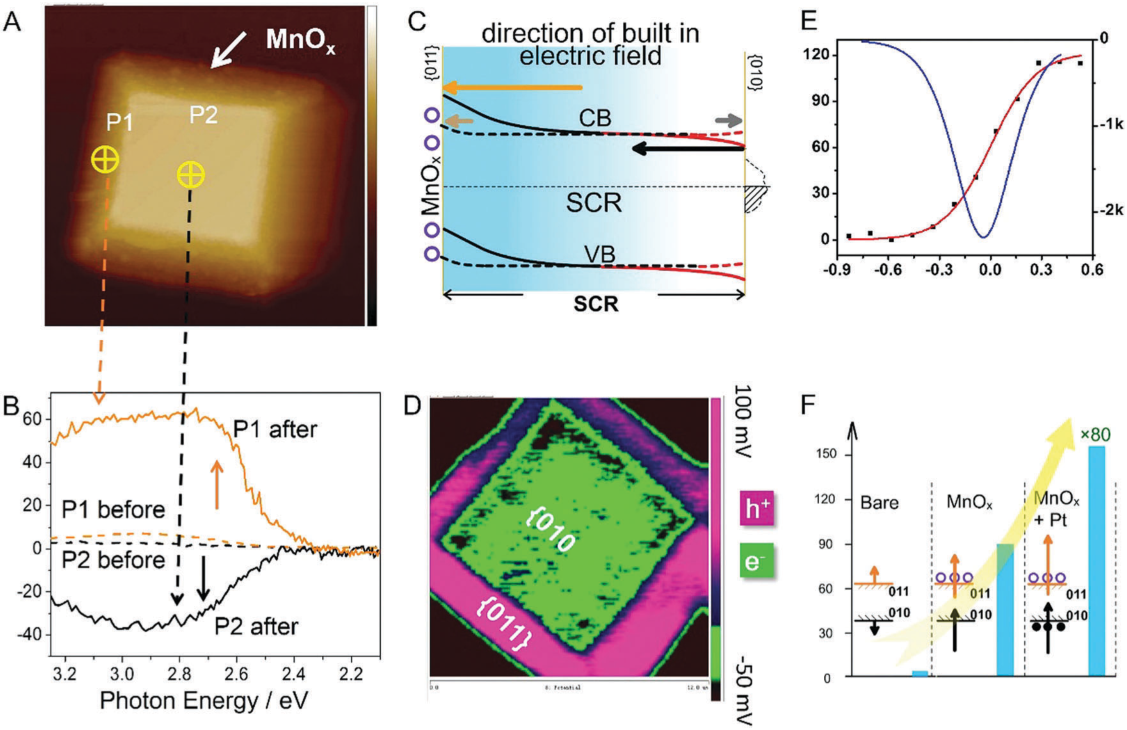

Fig. 17 (A) AFM topology image of a $BiVO_4$ single photocatalyst particle with facet-selectively photodeposited MnO_x nanoparticle on the {011} facets and (B) SRSPS obtained on the {010} and {011} facets before and after facet-selective cocatalyst deposition. (C) The direction of the built in electric field beneath the {010} facet was changed while the strength of the built in electric fields beneath the two facets was significantly increased. (D) Spatial distribution of the SPV signals of a single $BiVO_4$ photocatalyst particle with selectively deposited MnO_x and Pt cocatalyst at the {011} and {010} facets. (E) Maximum built-in electric field at the interface of up to 2.5 kV cm^{-1}. (F) Schematic showing the changes of the vectors of the built-in electric field in the bare cocatalyst and in the dual-cocatalyst deposited onto a $BiVO_4$ single photocatalyst particle. Adapted with permission from ref. 164. Copyright 2017, American Chemical Society.

the widths of the SCRs beneath both facets increased to several micrometers so that one common SCR with a strong additive built-in electric field was formed (Fig. 17C). The built-in electric field can be further enhanced by depositing Pt cocatalysts on the {010} facet. Fig. 17D shows the spatial distribution of the SPV signals of a single $BiVO_4$ photocatalyst particle with selectively deposited MnO_x and Pt cocatalysts at the {011} and {010} facets, respectively, which was obtained by the subtraction of KPFM images in the dark and under illumination, defined as SPVM. The positive signal in pink color stands for photogenerated holes and the negative signal in green color stands for photogenerated electrons separated towards the surface. It can be seen that the photogenerated electrons and holes are separated towards the border of the facets in a clear-cut fashion. The fitting of the cross section demonstrated that the maximum built-in electric field at the interface increased up to 2.5 kV cm^{-1}, which is of the same order as that of conventional silicon p–n junctions (Fig. 17E). Fig. 17F quantitatively summarizes the effects of cocatalysts on the vectors of the built-in electric field in the photocatalyst particle. For bare photocatalysts, the vector directions of built-in electric fields on the two facets are opposite to each other and the net driving force for charge separation (4 mV) is the difference of built-in electric fields on the two facets, which can be tuned by tailoring the morphology of the photocatalyst, as demonstrated in Fig. 16. The selective deposition of MnO_x cocatalysts on the {011} facets not only increased the built-in electric fields on the {011} facets but also changed the direction of built-in electric fields on the {001} facets, resulting in the same vector direction of the built-in electric fields on two types of facets and a strong net driving force for charge separation (100 mV) through the whole particle. The aligned driving force could be further enhanced to 170 mV after dual deposition of MnO_x and Pt on the {011} facets and {001} facets respectively.

This work revealed a decisive role of cocatalysts for charge separation: aligning the vectors of built-in electric fields to form strong additive built-in electric fields throughout the whole photocatalyst. The findings give deep insights into the design of highly efficient photocatalytic systems by aligning the distributions of built-in electric fields into an additive one with asymmetric cocatalyst assembly.

3.3.3 Buried electric field across a phase junction.

The fabrication of phase junction structures has been proven to be an effective strategy for promoting charge separation in solar fuel production.[17,18,166,167] In 2008, our group found that the photocatalytic activity of TiO_2 could be greatly enhanced when anatase TiO_2 nanoparticles were highly dispersed on the surface of rutile TiO_2 to form anatase–rutile surface-phase junctions.[17] Based on this concept, we further found that surface phase junctions on Ga_2O_3 can significantly improve the overall

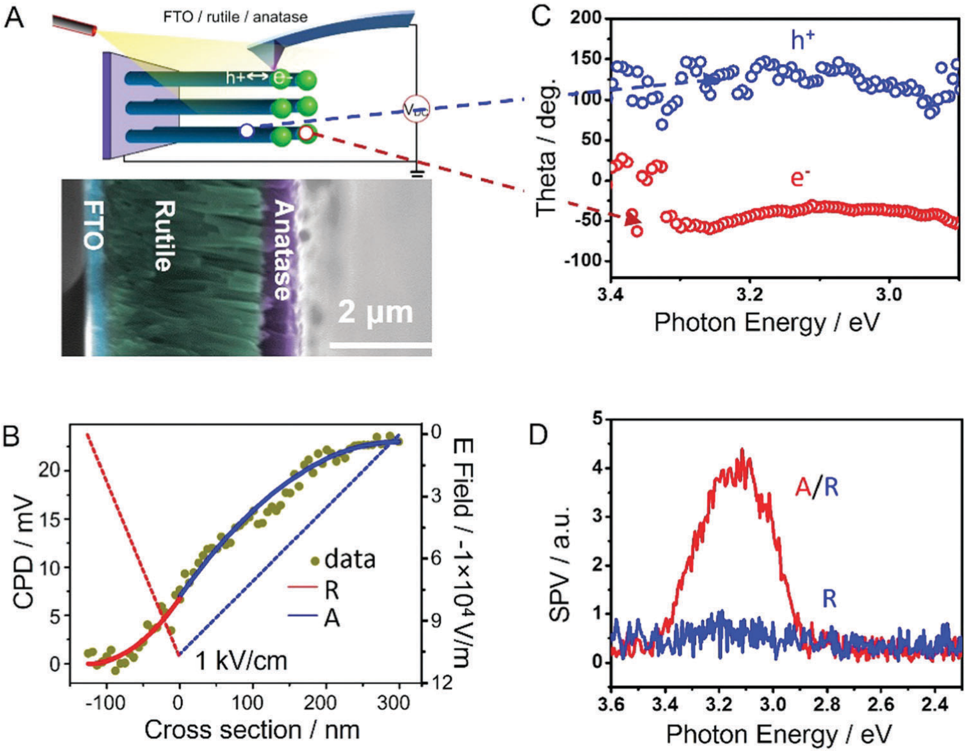

Fig. 18 (A) Setup of cross-section KPFM in order to obtain the energy band alignment at the rutile/anatase phase junction and cross section SEM image. (B) Cross section of the surface potential across the phase junction and differentiated fitting profile showing the maximum electric field of 1 kV cm^{-1}. (C) The phase and (D) amplitude SRSPS collected at the surface of rutile and anatase phases. Adapted with permission from ref. 169. Copyright 2017, American Chemical Society.

photocatalytic water splitting into H_2 and O_2.[18] In recent years, this concept has been successfully extended to the fabrication of PV devices[167] and PEC electrodes.[166] Despite the various proposed charge transfer processes derived from energy levels of pure anatase and rutile, convincing evidence for charge transfer and electric fields at the anatase/rutile junction is still lacking.[168] To address this issue, KPFM and SRSPS were employed to probe the interface of a model phase junction composed of rutile nanorods (NRs) and anatase nanoparticles (NPs).[169]

Fig. 18A shows the setup of cross-section KPFM to obtain the energy band alignment of a rutile/anatase phase junction. The rutile NRs were sputter coated with anatase NPs. The rutile/anatase sample was grounded *via* FTO without illumination and their Fermi levels were aligned at the thermal equilibrium state. Under this condition, CPD represents the variation of the local vacuum energy level relative to the Fermi level across the TiO_2 phase junctions. The cross section of the surface potential in Fig. 18B shows that the work function of rutile is 30 meV higher than that of anatase. This result is consistent with the widely accepted band alignment model of the rutile/anatase phase junction, although the absolute value is smaller than that obtained from pure phases.[170] Thus, an internal built-in electric field from anatase to rutile across the rutile/anatase junction can be formed. The fitting of the surface potential profile gave the concentration of charge carriers in rutile and anatase as 5.6×10^{18} cm^{-3} for NR and 1.2×10^{17} cm^{-3} for NA, respectively. The strength of the built-in electric field was obtained by differentiating the fitted profile and the maximum electric field was calculated to be ~1 kV cm^{-1}. The phase of SRSPS in Fig. 18C measured at the surface of rutile and anatase gave strong evidence that the accumulated photogenerated charge changed from holes to electrons after the formation of the phase junction (from 120° to −60°). The transfer of electrons from the rutile to the anatase phase is consistent with the direction of the built-in electric field, demonstrating that the drift dominates the charge separation. Moreover, the intensity of the SPV of mix-phase TiO_2 is about six times stronger than that of bare rutile NRs, as shown in Fig. 18D. This result reflects that phase junctions can significantly improve charge separation in comparison to the pure rutile phase. Another important parameter derived from Fig. 18B is that the depletion width of the anatase region should be about 300 nm. This number provides an interesting reference for experimental synthesis: it seems that the best size of anatase NPs should be around 300 nm, assuming that the drift length of photogenerated charge carriers will be of the same order. The reason for this may be ascribed to an ''incompletely depleted'' SCR below 300 nm and to recombination of photogenerated carriers outside the SCR.[76] This hypothesis is supported by the experimental fact that the SPV reached a maximum when the size reached 300 nm. This result provides a strong basis for understanding the impact of built-in electric fields on the charge transfer across the interface of photocatalysts with phase junctions.

3.3.4 Vectorial charge transfer in Z-scheme nanowires. Natural photosynthesis works with a Z-scheme mechanism in which two charge separation processes happen in two spatially separated photosystems connected in series with an electron transfer chain. This structure provides sufficient driving force for the chemical reactions and results in an extremely high quantum efficiency.[2] In artificial photosynthesis, the Z-scheme concept is well adapted and presented in the form of a reduction-evolving photocatalyst, an oxidation-evolving photocatalyst, and an electron mediator.[171,172] Most of the electron mediators are redox couples. In contrast, noble-metal nanoparticles are used in all-solid-state Z-schemes which are chemically stable and in which back reactions can be neglected. In such Z-schemes, intermediate electron–hole pairs recombine at the noble metal nanoparticles and another high energy electron–hole pair is saved.[173] To understand the function of such a system, the charge separation/transfer on a Z-scheme WO_3/Au/In_2S_3 nanowire array was probed on the nanoscale by using SPVM.[174]

Fig. 19A shows the precise construction of the Z-scheme structure. The photocatalytic reaction demonstrated that, with Au NPs as a mediator, the CH_4 evolution rate of WO_3/Au/In_2S_3 was 2.6 times higher than that of WO_3/In_2S_3. The KPFM measurements suggested the vectorial hole transfer of In_2S_3 → Au → WO_3 as shown by the band alignments in Fig. 19B. Fig. 19C and D show the SPVM images of the WO_3/In_2S_3 and WO_3/Au/In_2S_3 nanowires, respectively. The SPVM images are plotted for the same scale and clearly demonstrate that the positive SPV signal of a WO_3/Au/In_2S_3 nanowire is much higher than that of a WO_3/In_2S_3 nanowire (30 mV *vs.* 10 mV). As KPFM images are a weighted average of the surface potential underneath the tip apex, the changes of SPV signals should be mainly attributed to the increased concentration of photogenerated holes on the surface of the WO_3 nanowire, which possesses the largest surface area. As schematically shown in Fig. 18B, the recombination of photogenerated electrons and holes from the intermediate CB and VB levels in the Z-scheme keeps another electron–hole pair alive in a spatially separated fashion while enhancing the localized photovoltage and increasing the driving force for chemical reactions. The results indicate that the band alignments are the key factor for fabrication of solid Z-scheme photocatalytic systems and give insights into the superiority of the Z-scheme in charge separation compared with the direct heterojunctions.

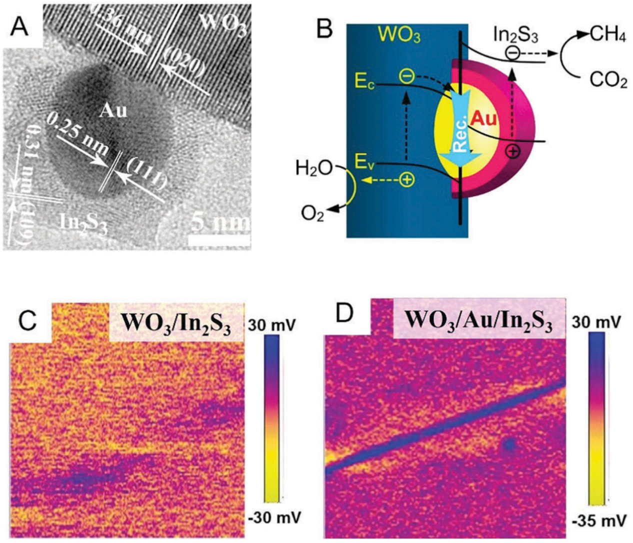

Fig. 19 (A) HRTEM image of the local structure of a Z-scheme WO_3/Au/In_2S_3 nanowire array. (B) Schematic showing the band alignment and charge separation process. SPVM images of the (C) WO_3/In_2S_3 and (D) WO_3/Au/In_2S_3 nanowires. Adapted with permission from ref. 174. Copyright 2016, American Chemical Society.

3.3.5 Positioning the water oxidation reaction site in plasmonic photocatalysts. The vivid optical properties of noble metal nanoparticles constituted by surface plasmon resonance (SPR) have given rise to diverse applications in photochemistry reactions, super-resolution spectroscopy, optical switching and biological sensing.[175–177] Due to its tunable spectral responses, incorporating a plasmonic nanostructure into semiconductor devices or catalysts led to the development of a new generation of hybrid nanostructures for desirable nanophotonic applications in solar energy conversion and storage.[178] In this respect, the specificities of plasmonic hybrid nanostructures with hot spots offer opportunities for optimizing a desired outcome and controlling photochemical reaction sites due to the possibility of optically-induced energy and charge migration across the interface.[179] A very challenging task in this field is how to localize the exact reaction site.

To understand this issue, we fabricated a plasmonic photocatalyst composed of Au NPs and TiO_2 (Fig. 20A)[180] and found that plasmonic water oxidation on Au/TiO_2 can be realized under irradiation of plasmonic absorption of light with a central wavelength of about 550 nm (Fig. 20B). The dark-state KPFM image presented a circle like belt region around the Au NPs, indicating that the surface potential of the interface between Au NPs and TiO_2 was 30 mV lower than that of TiO_2. This was ascribed to a Schottky junction at the interface of Au and TiO_2. More importantly, the SPVM image in Fig. 20C demonstrated an obvious circular ring at the interface. In contrast, the Au NPs and TiO_2 showed no changes. The detailed analysis of the SPVM image gave an increment of the SPV of +10 mV at the interface between Au and TiO_2, as shown in Fig. 20D. The following two conclusions could be drawn: holes generated by the plasmon resonance were readily accumulated at the interface between Au and TiO_2; the Schottky barrier at the interface was the key factor for promoting the transfer of hot electrons to TiO_2 and preventing them from recombining. These findings are further supported by a carefully designed experiment. It was found that the photocatalytic reaction rate could be significantly decreased by poisoning the interface between Au and TiO_2 with annealed CrO_x, as shown in Fig. 20B. The findings not only give clear evidence of where the hot holes distribute but also give deep insights into the role of the Schottky barrier at the Au/TiO_2 interface in promoting charge separation and stabilizing the hot holes.

3.3.6 New insights from spatially resolved SPV measurements on photocatalysts. Superior to the conventional SPV measurements

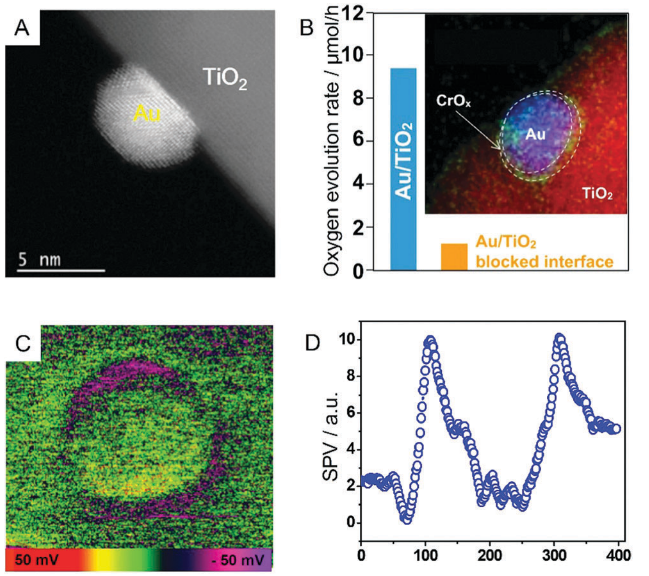

Fig. 20 (A) HAADF-STEM image of plasmonic photocatalysts composed of Au NPs and TiO_2. (B) Plasmonic water oxidation performance of the photocatalysts before and after interfacial block. (C) SPVM image of Au NP deposited on a TiO_2 rutile single crystal, obtained by subtracting the surface potential under dark conditions from that under illumination at a wavelength of 532 nm. (D) SPV profile across the Au/TiO_2 composite particle. Adapted with permission from ref. 180. Copyright 2017, American Chemical Society.

on photocatalyst aggregations, spatially resolved SPV techniques allow quantitative SPV measurements on a single photocatalyst particle. New insights into promoting charge separation have been provided by the spatial heterogeneity of surface potential and SPV distributions on single photocatalyst particles or nanostructures.

Fig. 21 schematically compares the charge separation in photoelectrochemistry (PEC) and photocatalysis. For a PEC cell (Fig. 21A), the photogenerated holes are separated to the surface of a photoanode by an electric field that is formed at or near the semiconductor/liquid interface and the photogenerated electrons are transferred to a counter electrode *via* an external circuit by an applied bias.[181] Meanwhile, charge separation in suspended photocatalyst particles is much more of a challenge as the photogenerated electrons and holes are required to be separated to different surface locations of the photocatalyst in such a small space (nm–μm) without an external driving force. The symmetric built-in electric fields surrounding the photocatalyst particle make the matter worse.[76] As demonstrated by the SPVM on photocatalyst particles (Fig. 10),[125] the surface built-in electric fields only drive the photogenerated minority carriers to the surface but act as a surface barrier for the photogenerated majority carriers, thus strongly limiting the charge separation and photocatalytic performance.[182,183] Using a vectorial viewpoint, the symmetric built-in electric fields surrounding the photocatalyst cancel each other out, and no net driving force can be produced in the photocatalyst particle (Fig. 21B). Taking advantage of SRSPS, we found that the surface built-in electric fields are highly anisotropic on different facets of a single photocatalyst particle (Fig. 16).[108] The net driving force for charge separation can be produced by the difference between the built-in electric fields on different facets (Fig. 21C), which can be enhanced by tuning the morphology of the photocatalyst particle. The symmetry of the surface built-in electric fields can be further broken by the asymmetric assembly of cocatalysts (Fig. 21D). Using SRSPS and SPVM, we showed that the selective deposition of MnOx cocatalysts on the {011} facets of a $BiVO_4$ photocatalyst particle

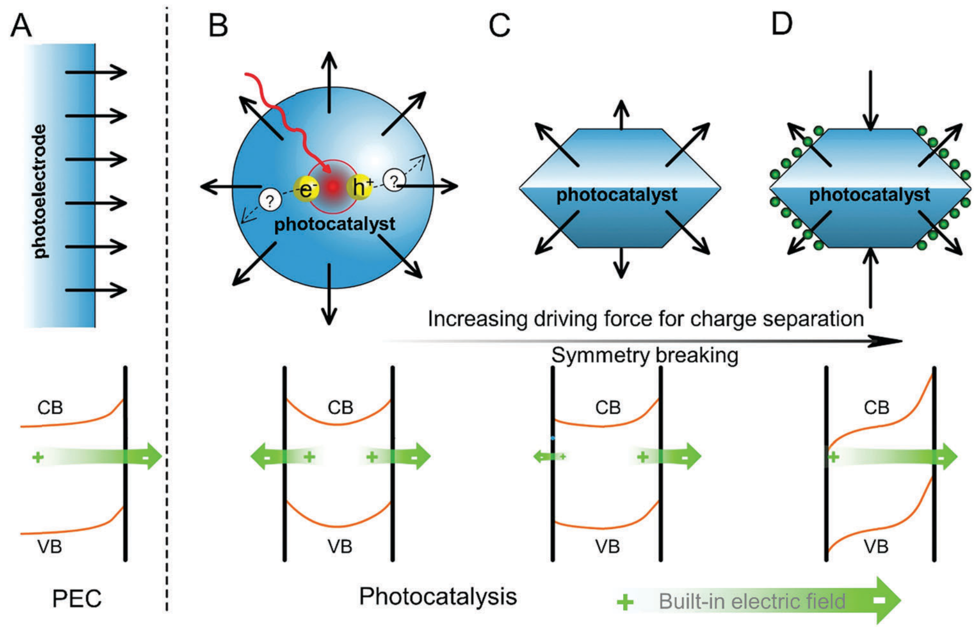

Fig. 21 Schematic showing the driving force for charge separation in (A) PEC and photocatalyst particles with (B) symmetric built-in electric fields, (C) anisotropic built-in electric fields on different facets and (D) asymmetric cocatalyst assembly.

not only increases the built-in electric fields on the {011} facets but also inverts the direction of the built-in electric fields on the {001} facets (Fig. 17).[164] In this case, the vectorial direction of the built-in electric fields on the {011} facets and {001} facets is the same and a strong aligned driving force can be formed throughout the whole photocatalyst particle to efficiently separate the photocatalyst charges. Besides, the asymmetric built-in electric fields can also be created by fabricating phase junctions (Fig. 18), heterojunctions (Fig. 19) or Schottky interfaces (Fig. 20). The strength, direction and scale of the asymmetric built-in electric fields can be determined by the spatially resolved SPV technique combined with KPFM, thus giving deep insights into the optimization of these asymmetric built-in electric fields. All these insights highlight the significant importance of breaking the symmetry of built-in electric fields and creating an aligned driving force for highly efficient charge separation.

4. Summary and outlook

Photoinduced charge transfer across the nanometer to micrometer scale, with varied lifetime, constitutes the key factor in photocatalytic solar to fuel conversion. Advancing these catalysts towards high photo to chemical conversion efficiency requires an understanding of the photogenerated charge separation and transfer process. Tracing back to the physics of the charge separation, it is the built-in electrical fields beneath the surface or buried at the interface of the photocatalyst that provide the driving force. The surface photovoltage (SPV) technique has been demonstrated to be a useful tool for studying CST processes in photocatalytic systems. In this review, the SPV principle was explained with regard to charge separation across a SCR in a depletion layer at a semiconductor surface, and the center of charge approach, the relaxation of SPV signals and the measurement of SPV signals with conventional Kelvin probes and with fixed capacitors were described. As examples complementary to spatially resolved SPV techniques, advances in transient SPV for understanding time-dependent charge separation were given.

The principle of spatially resolved SPV techniques is based on the nm-scale measurement of the local surface potential and the light-induced surface potential changes (SPV) using KPFM combined with modulated illumination systems. The techniques allow nanoscale spatial resolution and mV energy sensitivity, opening a new powerful way for studying the local charge separation in photocatalysis.

Making use of these tools, important progress has been made in the past several years. The role of built-in electric fields in the SCR of different facets played in the anisotropic photoinduced charge transfer in a single crystal $BiVO_4$ photocatalyst is clearly revealed; the local separation of photogenerated charge carriers across cocatalyst loaded photocatalyst particles was probed. We found that the cocatalyst has a conclusive effect on charge separation in photocatalyst particles by aligning the vectors of built-in electric fields in the photocatalyst particle; a built-in electric field of up to 1 kV cm^{-1} across the rutile/anatase interface was quantitatively probed, driving the photogenerated electrons transferred from rutile nanorods (NRs) to anatase nanoparticles (NPs) under UV light illumination. We clearly demonstrated that the plasmon-induced water oxidation reaction takes place at the reaction sites localized at the interface between Au and TiO_2, and the distribution of holes is probed by surface photovoltage imaging. These results not only demonstrate the nature of driving force for charge separation in a single semiconductor photocatalyst particle but also give new insights into how to create and enhance the driving force. The driving force is determined by the aligned built-in electric fields that can be enhanced by asymmetric facet engineering, asymmetric cocatalyst assembly or asymmetric junction fabrication. The new insights provide an exciting opportunity to rationally design highly efficient photocatalytic systems.

For the future, an extension of SPV imaging techniques towards *in situ* or *in operando* experiments with photocatalysts is expected. In this respect, Bard and Boettcher have made efforts to develop nm-scale scanning electrochemical potential microscopy (SECM) to probe the electrical and interfacial properties of heterogeneous (photo) electrochemical systems.[184–187] It is not very risky to predict that the nm-scale SECM will also become important in understanding the driving forces for solar fuel production under real conditions. Another important feature of photocatalysts for solar fuel production is the widespread distribution of charge carrier's lifetime. However, the extension of the time range for the investigation of the photo-induced ΔCPD by SPV imaging techniques is still challenging,[188] so that a combination of imaging SPV techniques providing excellent resolution in space with SPV measurements in fixed capacitor arrangements allowing for a large time range is very useful. Alternatively, developing time-resolved SPV imaging techniques is an interesting future avenue.[189–192] Developments are also incessantly continuing towards increased accuracy, sensitivity and spatial resolution of SPV imaging techniques to meet a wide variety of advanced materials.[193] We have no doubt that further development of SPV imaging techniques will open an array of new research opportunities to understand photocatalysis for solar energy conversion.

Conflicts of interest

There are no conflicts to declare.

Acknowledgements

This work was supported by the National Natural Science Foundation of China (Grant No. 21633015, 21773228), the National Key Basic Research Program of China (973 Program, Grant No. 2014CB239403), and the Strategic Priority Research Program and Equipment Development Project of the Chinese Academy of Sciences (Grant No. XDB17000000, YJKYYQ20170002).

References

1 N. S. Lewis, *Science*, 2016, **351**, aad1920.
2 Y. Tachibana, L. Vayssieres and J. R. Durrant, *Nat. Photonics*, 2012, **6**, 511.
3 D. Gust, T. A. Moore and A. L. Moore, *Acc. Chem. Res.*, 2009, **42**, 1890.
4 J. J. Concepcion, R. L. House, J. M. Papanikolas and T. J. Meyer, *Proc. Natl. Acad. Sci. U. S. A.*, 2012, **109**, 15560.
5 Q. Wang, T. Hisatomi, Q. Jia, H. Tokudome, M. Zhong, C. Wang, Z. Pan, T. Takata, M. Nakabayashi, N. Shibata, Y. Li, I. D. Sharp, A. Kudo, T. Yamada and K. Domen, *Nat. Mater.*, 2016, **15**, 611.
6 S. Chen, T. Takata and K. Domen, *Nat. Rev. Mater.*, 2017, **2**, 17050.
7 B. A. Pinaud, J. D. Benck, L. C. Seitz, A. J. Forman, Z. Chen, T. G. Deutsch, B. D. James, K. N. Baum, G. N. Baum, S. Ardo, H. Wang, E. Miller and T. F. Jaramillo, *Energy Environ. Sci.*, 2013, **6**, 1983.
8 D. M. Fabian, S. Hu, N. Singh, F. A. Houle, T. Hisatomi, K. Domen, F. E. Osterloh and S. Ardo, *Energy Environ. Sci.*, 2015, **8**, 2825.
9 J. H. Yang, D. G. Wang, H. X. Han and C. Li, *Acc. Chem. Res.*, 2013, **46**, 1900.
10 T. Hisatomi, J. Kubota and K. Domen, *Chem. Soc. Rev.*, 2014, **43**, 7520.
11 Y. X. Xu, A. L. Li, T. T. Yao, C. T. Ma, X. W. Zhang, J. H. Shah and H. X. Han, *ChemSusChem*, 2017, **10**, 4277.
12 S. Bai, J. Jiang, Q. Zhang and Y. J. Xiong, *Chem. Soc. Rev.*, 2015, **44**, 2893.
13 Z. Li, J. Feng, S. Yan and Z. Zou, *Nano Today*, 2015, **10**, 468.
14 H. L. Wang, L. S. Zhang, Z. G. Chen, J. Q. Hu, S. J. Li, Z. H. Wang, J. S. Liu and X. C. Wang, *Chem. Soc. Rev.*, 2014, **43**, 5234.
15 S. J. A. Moniz, S. A. Shevlin, D. J. Martin, Z. X. Guo and J. W. Tang, *Energy Environ. Sci.*, 2015, **8**, 731.
16 J. Low, J. Yu, M. Jaroniec, S. Wageh and A. A. Al-Ghamdi, *Adv. Mater.*, 2017, **29**, 1601694.
17 J. Zhang, Q. Xu, Z. Feng, M. Li and C. Li, *Angew. Chem., Int. Ed.*, 2008, **47**, 1766.
18 X. Wang, Q. Xu, M. Li, S. Shen, X. Wang, Y. Wang, Z. Feng, J. Shi, H. Han and C. Li, *Angew. Chem., Int. Ed.*, 2012, **51**, 13089.
19 F. E. Osterloh, *Chem. Soc. Rev.*, 2013, **42**, 2294.
20 H. Zhou, Y. Qu, T. Zeid and X. Duan, *Energy Environ. Sci.*, 2012, **5**, 6732.
21 R. Li, F. Zhang, D. Wang, J. Yang, M. Li, J. Zhu, X. Zhou, H. Han and C. Li, *Nat. Commun.*, 2013, **4**, 1432.
22 G. Liu, H. G. Yang, J. Pan, Y. Q. Yang, G. Q. Lu and H. M. Cheng, *Chem. Rev.*, 2014, **114**, 9559.
23 J. R. Ran, J. Zhang, J. G. Yu, M. Jaroniec and S. Z. Qiao, *Chem. Soc. Rev.*, 2014, **43**, 7787.
24 J. B. Baxter, C. Richter and C. A. Schmuttenmaer, *Annu. Rev. Phys. Chem.*, 2014, **65**, 423.
25 A. J. Cowan and J. R. Durrant, *Chem. Soc. Rev.*, 2013, **42**, 2281.
26 K. Tvrdy, P. A. Frantsuzov and P. V. Kamat, *Proc. Natl. Acad. Sci. U. S. A.*, 2011, **108**, 29.
27 Y. Yang, J. Gu, J. L. Young, E. M. Miller, J. A. Turner, N. R. Neale and M. C. Beard, *Science*, 2015, **350**, 1061.
28 D. V. Esposito, J. B. Baxter, J. John, N. S. Lewis, T. P. Moffat, T. Ogitsu, G. D. O'Neil, T. A. Pham, A. A. Talin, J. M. Velazquez and B. C. Wood, *Energy Environ. Sci.*, 2015, **8**, 2863.
29 C. X. Kronawitter, L. Vayssieres, S. Shen, L. Guo, D. A. Wheeler, J. Z. Zhang, B. R. Antoun and S. S. Mao, *Energy Environ. Sci.*, 2011, **4**, 3889.
30 M. Barroso, C. A. Mesa, S. R. Pendlebury, A. J. Cowan, T. Hisatomi, K. Sivula, M. Gratzel, D. R. Klug and J. R. Durrant, *Proc. Natl. Acad. Sci. U. S. A.*, 2012, **109**, 15640.
31 L. M. Carneiro, S. K. Cushing, C. Liu, Y. Su, P. Yang, A. P. Alivisatos and S. R. Leone, *Nat. Mater.*, 2017, **16**, 819.
32 J. E. Katz, X. Y. Zhang, K. Attenkofer, K. W. Chapman, C. Frandsen, P. Zarzycki, K. M. Rosso, R. W. Falcone, G. A. Waychunas and B. Gilbert, *Science*, 2012, **337**, 1200.
33 M. H. Rittmann-Frank, C. J. Milne, J. Rittmann, M. Reinhard, T. J. Penfold and M. Chergui, *Angew. Chem., Int. Ed.*, 2014, **53**, 5858.
34 X. Liu, G. Dong, S. Li, G. Lu and Y. Bi, *J. Am. Chem. Soc.*, 2016, **138**, 2917.
35 T. Tachikawa and T. Majima, *Chem. Soc. Rev.*, 2010, **39**, 4802.
36 J. B. Sambur, T. Y. Chen, E. Choudhary, G. Chen, E. J. Nissen, E. M. Thomas, N. Zou and P. Chen, *Nature*, 2016, **530**, 77.
37 T. Chen, B. Dong, K. Chen, F. Zhao, X. Cheng, C. Ma, S. Lee, P. Zhang, S. H. Kang, J. W. Ha, W. Xu and N. Fang, *Chem. Rev.*, 2017, **117**, 7510.
38 A. Yurtsever, R. M. van der Veen and A. H. Zewail, *Science*, 2012, **335**, 59.
39 E. Najafi, T. D. Scarborough, J. Tang and A. Zewail, *Science*, 2015, **347**, 164.
40 G. M. Vanacore, A. W. P. Fitzpatrick and A. H. Zewail, *Nano Today*, 2016, **11**, 228.
41 S. Schafer, Z. Wang, R. Zierold, T. Kipp and A. Mews, *Nano Lett.*, 2011, **11**, 2672.
42 S. C. Warren, K. Voitchovsky, H. Dotan, C. M. Leroy, M. Cornuz, F. Stellacci, C. Hebert, A. Rothschild and M. Gratzel, *Nat. Mater.*, 2013, **12**, 842.
43 R. Giridharagopal, P. A. Cox and D. S. Ginger, *Acc. Chem. Res.*, 2016, **49**, 1769.
44 H. C. Gatos and J. Lagowski, *J. Vac. Sci. Technol.*, 1973, **10**, 130.
45 J. Lagowski, I. Baltov and H. C. Gatos, *Surf. Sci.*, 1973, **40**, 216.
46 J. Lagowski, E. S. Sproles and H. C. Gatos, *J. Appl. Phys.*, 1977, **48**, 3566.
47 J. Lagowski, *Surf. Sci.*, 1994, **299**, 92.
48 L. Kronik and Y. Shapira, *Surf. Sci. Rep.*, 1999, **37**, 1.
49 L. Jing, X. Sun, J. Shang, W. Cai, Z. Xu, Y. Du and H. Fu, *Sol. Energy Mater. Sol. Cells*, 2003, **79**, 133.
50 I. Mora-Seró, T. Dittrich, G. Garcia-Belmonte and J. Bisquert, *J. Appl. Phys.*, 2006, **100**, 103705.

51 D. Gross, I. Mora-Sero, T. Dittrich, A. Belaidi, C. Mauser, A. J. Houtepen, E. Da Como, A. L. Rogach and J. Feldmann, *J. Am. Chem. Soc.*, 2010, **132**, 5981.

52 J. Zhao and F. E. Osterloh, *J. Phys. Chem. Lett.*, 2014, **5**, 782.

53 J. Zhao, B. A. Nail, M. A. Holmes and F. E. Osterloh, *J. Phys. Chem. Lett.*, 2016, **7**, 3335.

54 S. Li, L. Hou, L. Zhang, L. Chen, Y. Lin, D. Wang and T. Xie, *J. Mater. Chem. A*, 2015, **3**, 17820.

55 T. Dittrich, I. Mora-Seró, G. García-Belmonte and J. Bisquert, *Phys. Rev. B: Condens. Matter Mater. Phys.*, 2006, **73**, 045407.

56 J. A. Anta, I. Mora-Sero, T. Dittrich and J. Bisquert, *J. Phys. Chem. C*, 2007, **111**, 13997.

57 X. Jiao, Z. Chen, X. Li, Y. Sun, S. Gao, W. Yan, C. Wang, Q. Zhang, Y. Lin, Y. Luo and Y. Xie, *J. Am. Chem. Soc.*, 2017, **139**, 7586.

58 S. Ye, R. Chen, Y. Xu, F. Fan, P. Du, F. Zhang, X. Zong, T. Chen, Y. Qi, P. Chen, Z. Chen and C. Li, *J. Catal.*, 2016, **338**, 168.

59 Y. Luan, L. Jing, Y. Xie, X. Sun, Y. Feng and H. Fu, *ACS Catal.*, 2013, **3**, 1378.

60 T. Dittrich, S. Fengler and M. Franke, *Rev. Sci. Instrum.*, 2017, **88**, 053904.

61 T. Dittrich, L. E. Valle Rios, S. Kapil, G. Gurieva, N. Rujisamphan and S. Schorr, *Appl. Phys. Lett.*, 2017, **110**, 023901.

62 M. A. Reshchikov, M. Foussekis and A. A. Baski, *J. Appl. Phys.*, 2010, **107**, 113535.

63 T. K. Townsend, N. D. Browning and F. E. Osterloh, *Energy Environ. Sci.*, 2012, **5**, 9543.

64 L. Jing, W. Zhou, G. Tian and H. Fu, *Chem. Soc. Rev.*, 2013, **42**, 9509.

65 F. A. Frame, T. K. Townsend, R. L. Chamousis, E. M. Sabio, T. Dittrich, N. D. Browning and F. E. Osterloh, *J. Am. Chem. Soc.*, 2011, **133**, 7264.

66 J. Wang, J. Zhao and F. E. Osterloh, *Energy Environ. Sci.*, 2015, **8**, 2970.

67 B. A. Nail, J. M. Fields, J. Zhao, J. R. Wang, M. J. Greaney, R. L. Brutchey and F. E. Osterloh, *ACS Nano*, 2015, **9**, 5135.

68 M. Xie, X. Fu, L. Jing, P. Luan, Y. Feng and H. Fu, *Adv. Energy Mater.*, 2014, **4**, 1300995.

69 X. Zhang, L. Z. Zhang, T. F. Xie and D. J. Wang, *J. Phys. Chem. C*, 2009, **113**, 7371.

70 L. Peng, T. Xie, Y. Lu, H. Fan and D. Wang, *Phys. Chem. Chem. Phys.*, 2010, **12**, 8033.

71 W. H. Brattain, *Phys. Rev.*, 1947, **72**, 345.

72 W. H. Brattain and J. Bardeen, *AT&T Tech. J.*, 1953, **32**, 1.

73 C. G. B. Garrett and W. H. Brattain, *Phys. Rev.*, 1955, **99**, 376.

74 D. K. Schroder, *Meas. Sci. Technol.*, 2001, **12**, R16.

75 L. Li, P. A. Salvador and G. S. Rohrer, *Nanoscale*, 2014, **6**, 24.

76 Z. Zhang and J. T. Yates, Jr., *Chem. Rev.*, 2012, **112**, 5520.

77 S. Bai, L. Wang, Z. Li and Y. Xiong, *Adv. Sci.*, 2017, **4**, 1600216.

78 H. Dember, *Phys. Z.*, 1931, **32**, 554.

79 S. R. Goldman, K. Kalikstein and B. Kramer, *J. Appl. Phys.*, 1978, **49**, 2849.

80 H. J. Mandujano-Ramirez, J. P. Gonzalez-Vazquez, G. Oskam, T. Dittrich, G. Garcia-Belmonte, I. Mora-Sero, J. Bisquert and J. A. Anta, *Phys. Chem. Chem. Phys.*, 2014, **16**, 4082.

81 E. O. Johnson, *J. Appl. Phys.*, 1957, **28**, 1349.

82 K. Heilig, *Surf. Sci.*, 1974, **44**, 421.

83 V. Duzhko, F. Koch and T. Dittrich, *J. Appl. Phys.*, 2002, **91**, 9432.

84 T. Dittrich, S. Bonisch, P. Zabel and S. Dube, *Rev. Sci. Instrum.*, 2008, **79**, 113903.

85 T. Dittrich, S. Fiechter and A. Thomas, *Appl. Phys. Lett.*, 2011, **99**, 084105.

86 M. A. Melo, Jr., Z. Wu, B. A. Nail, A. T. De Denko, A. F. Nogueira and F. E. Osterloh, *Nano Lett.*, 2018, **18**, 805.

87 T. T. Yao, R. T. Chen, J. J. Li, J. F. Han, W. Qin, H. Wang, J. Y. Shi, F. T. Fan and C. Li, *J. Am. Chem. Soc.*, 2016, **138**, 13664.

88 S. Ye, C. Ding, R. Chen, F. Fan, P. Fu, H. Yin, X. Wang, Z. Wang, P. Du and C. Li, *J. Am. Chem. Soc.*, 2018, **140**, 3250.

89 V. Duzhko, V. Y. Timoshenko, F. Koch and T. Dittrich, *Phys. Rev. B: Condens. Matter Mater. Phys.*, 2001, **64**, 075204.

90 I. Mora-Sero, D. Gross, T. Mittereder, A. A. Lutich, A. S. Susha, T. Dittrich, A. Belaidi, R. Caballero, F. Langa, J. Bisquert and A. L. Rogach, *Small*, 2010, **6**, 221.

91 S. Fengler and T. Dittrich, *J. Phys. Chem. C*, 2016, **120**, 17777.

92 L. J. Zhang, S. Li, B. K. Liu, D. J. Wang and T. F. Xie, *ACS Catal.*, 2014, **4**, 3724.

93 J. Jiang, X. Zhang, P. Sun and L. Zhang, *J. Phys. Chem. C*, 2011, **115**, 20555.

94 X. Wei, T. Xie, L. Peng, W. Fu, J. Chen, Q. Gao, G. Hong and D. Wang, *J. Phys. Chem. C*, 2011, **115**, 8637.

95 L. He, L. Jing, Y. Luan, L. Wang and H. Fu, *ACS Catal.*, 2014, **4**, 990.

96 D. Xu, T. Jiang, D. Wang, L. Chen, L. Zhang, Z. Fu, L. Wang and T. Xie, *ACS Appl. Mater. Interfaces*, 2014, **6**, 9321.

97 L. Bi, D. Meng, Q. Bu, Y. Lin, D. Wang and T. Xie, *Phys. Chem. Chem. Phys.*, 2016, **18**, 31534.

98 I. Mora-Sero, J. Bisquert, T. Dittrich, A. Belaidi, A. S. Susha and A. L. Rogach, *J. Phys. Chem. C*, 2007, **111**, 14889.

99 E. Zillner and T. Dittrich, *Phys. Status Solidi RRL*, 2011, **5**, 256.

100 S. Fengler, E. Zillner and T. Dittrich, *J. Phys. Chem. C*, 2013, **117**, 6462.

101 Z. J. Han, F. Qiu, R. Eisenberg, P. L. Holland and T. D. Krauss, *Science*, 2012, **338**, 1321.

102 Y. M. Fang, Z. M. Li, Y. Y. Jiang, X. Wang, H. Y. Chen, N. J. Tao and W. Wang, *Proc. Natl. Acad. Sci. U. S. A.*, 2017, **114**, 10566.

103 E. Zillner, S. Fengler, P. Niyamakom, F. Rauscher, K. Köhler and T. Dittrich, *J. Phys. Chem. C*, 2012, **116**, 16747.

104 G. Binnig, C. F. Quate and C. Gerber, *Phys. Rev. Lett.*, 1986, **56**, 930.

105 E. M. Tennyson, C. Gong and M. S. Leite, *ACS Energy Lett.*, 2017, **2**, 2761.

106 M. Nonnenmacher, M. P. O'Boyle and H. K. Wickramasinghe, *Appl. Phys. Lett.*, 1991, **58**, 2921.

107 F. Streicher, S. Sadewasser and M. Lux-Steiner, *Rev. Sci. Instrum.*, 2009, **80**, 013907.

108 J. Zhu, F. Fan, R. Chen, H. An, Z. Feng and C. Li, *Angew. Chem., Int. Ed.*, 2015, **54**, 9111.

109 J. L. Luria, N. Hoepker, R. Bruce, A. R. Jacobs, C. Groves and J. A. Marohn, *ACS Nano*, 2012, **6**, 9392.

110 E. M. Tennyson, J. L. Garrett, J. A. Frantz, J. D. Myers, R. Y. Bekele, J. S. Sanghera, J. N. Munday and M. S. Leite, *Adv. Energy Mater.*, 2015, **5**, 1501142.

111 Y. Almadori, N. Bendiab and B. Grevin, *ACS Appl. Mater. Interfaces*, 2018, **10**, 1363.

112 E. J. Spadafora, R. Demadrille, B. Ratier and B. Grevin, *Nano Lett.*, 2010, **10**, 3337.

113 C. Barth, A. S. Foster, C. R. Henry and A. L. Shluger, *Adv. Mater.*, 2011, **23**, 477.

114 A. Liscio, V. Palermo and P. Samori, *Acc. Chem. Res.*, 2010, **43**, 541.

115 G. H. Enevoldsen, T. Glatzel, M. C. Christensen, J. V. Lauritsen and F. Besenbacher, *Phys. Rev. Lett.*, 2008, **100**, 236104.

116 W. Melitz, J. Shen, A. C. Kummel and S. Lee, *Surf. Sci. Rep.*, 2011, **66**, 1.

117 L. Kelvin, *Philos. Mag.*, 1898, **46**, 82.

118 W. A. Zisman, *Rev. Sci. Instrum.*, 1932, **3**, 367.

119 M. Liu, J. L. Lyons, D. Yan and M. S. Hybertsen, *Adv. Funct. Mater.*, 2016, **26**, 219.

120 F. F. Abdi, L. Han, A. H. Smets, M. Zeman, B. Dam and R. van de Krol, *Nat. Commun.*, 2013, **4**, 2195.

121 H. Hoppe, T. Glatzel, M. Niggemann, A. Hinsch, M. C. Lux-Steiner and N. S. Sariciftci, *Nano Lett.*, 2005, **5**, 269.

122 V. W. Bergmann, S. A. Weber, F. Javier Ramos, M. K. Nazeeruddin, M. Gratzel, D. Li, A. L. Domanski, I. Lieberwirth, S. Ahmad and R. Berger, *Nat. Commun.*, 2014, **5**, 5001.

123 J. B. Li, V. Chawla and B. M. Clemens, *Adv. Mater.*, 2012, **24**, 720.

124 F. Fuchs, F. Caffy, R. Demadrille, T. Melin and B. Grevin, *ACS Nano*, 2016, **10**, 739.

125 R. Chen, J. Zhu, H. An, F. Fan and C. Li, *Faraday Discuss.*, 2017, **198**, 473.

126 M. Hara, T. Kondo, M. Komoda, S. Ikeda, K. Shinohara, A. Tanaka, J. N. Kondo and K. Domen, *Chem. Commun.*, 1998, 357.

127 A. Kudo, K. Omori and H. Kato, *J. Am. Chem. Soc.*, 1999, **121**, 11459.

128 A. Paracchino, V. Laporte, K. Sivula, M. Gratzel and E. Thimsen, *Nat. Mater.*, 2011, **10**, 456.

129 T. W. Kim and K. S. Choi, *Science*, 2014, **343**, 990.

130 R. G. Li, X. P. Tao, R. T. Chen, F. T. Fan and C. Li, *Chem. – Eur. J.*, 2015, **21**, 14337.

131 G. Z. Shao, M. S. Glaz, F. Ma, H. X. Ju and D. S. Ginger, *ACS Nano*, 2014, **8**, 10799.

132 Y. C. Kim, N. J. Jeon, J. H. Noh, W. S. Yang, J. Seo, J. S. Yun, A. Ho-Baillie, S. Huang, M. A. Green, J. Seidel, T. K. Ahn and S. I. Seok, *Adv. Energy Mater.*, 2016, **6**, 1502104.

133 A. Winnerl, R. N. Pereira and M. Stutzmann, *Phys. Rev. B: Condens. Matter Mater. Phys.*, 2015, **91**, 075316.

134 R. B. Darling, *Phys. Rev. B: Condens. Matter Mater. Phys.*, 1991, **43**, 4071.

135 C. Sommerhalter, T. Glatzel, T. W. Matthes, A. Jager-Waldau and M. C. Lux-Steiner, *Appl. Surf. Sci.*, 2000, **157**, 263.

136 F. Krok, K. Sajewicz, J. Konior, M. Goryl, P. Piatkowski and M. Szymonski, *Phys. Rev. B: Condens. Matter Mater. Phys.*, 2008, **77**, 235427.

137 V. Donchev, K. Kirilov, T. Ivanov and K. Germanova, *Mater. Sci. Eng., B*, 2006, **129**, 186.

138 X. Zong, H. J. Yan, G. P. Wu, G. J. Ma, F. Y. Wen, L. Wang and C. Li, *J. Am. Chem. Soc.*, 2008, **130**, 7176.

139 H. Kato, K. Asakura and A. Kudo, *J. Am. Chem. Soc.*, 2003, **125**, 3082.

140 S. J. Tan, A. Argondizzo, J. D. Ren, L. M. Liu, J. Zhao and H. Petek, *Nat. Photonics*, 2017, **11**, 806.

141 Q. Chen, L. Mao, Y. W. Li, T. Kong, N. Wu, C. Q. Ma, S. Bai, Y. Z. Jin, D. Wu, W. Lu, B. Wang and L. W. Chen, *Nat. Commun.*, 2015, **6**, 7745.

142 S. U. Nanayakkara, J. van de Lagemaat and J. M. Luther, *Chem. Rev.*, 2015, **115**, 8157.

143 S. U. Nanayakkara, G. Cohen, C. S. Jiang, M. J. Romero, K. Maturova, M. Al-Jassim, J. van de Lagemaat, Y. Rosenwaks and J. M. Luther, *Nano Lett.*, 2013, **13**, 1278.

144 S. Lee, C. W. Liang and L. W. Martin, *ACS Nano*, 2011, **5**, 3736.

145 L. Dou, M. L. Lai, C. S. Kley, Y. M. Yang, C. G. Bischak, D. D. Zhang, S. W. Eaton, N. S. Ginsberg and P. D. Yang, *Proc. Natl. Acad. Sci. U. S. A.*, 2017, **114**, 7216.

146 H. Yoo, C. Bae, Y. Yang, S. Lee, M. Kim, H. Kim, Y. Kim and H. Shin, *Nano Lett.*, 2014, **14**, 4413.

147 N. J. Economou, S. Mubeen, S. K. Buratto and E. W. McFarland, *Nano Lett.*, 2014, **14**, 3328.

148 S. H. Lee, S. W. Lee, T. Oh, S. H. Petrosko, C. A. Mirkin and J. W. Jang, *Nano Lett.*, 2018, **18**, 109.

149 G. Liu, J. C. Yu, G. Q. Lu and H. M. Cheng, *Chem. Commun.*, 2011, **47**, 6763.

150 A. Vittadini, A. Selloni, F. P. Rotzinger and M. Gratzel, *Phys. Rev. Lett.*, 1998, **81**, 2954.

151 M. Lazzeri, A. Vittadini and A. Selloni, *Phys. Rev. B: Condens. Matter Mater. Phys.*, 2001, **63**, 155409.

152 G. S. Herman, M. R. Sievers and Y. Gao, *Phys. Rev. Lett.*, 2000, **84**, 3354.

153 X. Q. Gong and A. Selloni, *J. Phys. Chem. B*, 2005, **109**, 19560.

154 H. G. Yang, C. H. Sun, S. Z. Qiao, J. Zou, G. Liu, S. C. Smith, H. M. Cheng and G. Q. Lu, *Nature*, 2008, **453**, 638.

155 T. Ohno, K. Sarukawa and M. Matsumura, *New J. Chem.*, 2002, **26**, 1167.

156 T. Tachikawa, S. Yamashita and T. Majima, *J. Am. Chem. Soc.*, 2011, **133**, 7197.

157 L. L. Wang, J. Ge, A. L. Wang, M. S. Deng, X. J. Wang, S. Bai, R. Li, J. Jiang, Q. Zhang, Y. Luo and Y. J. Xiong, *Angew. Chem., Int. Ed.*, 2014, **53**, 5107.

158 G. C. Xi and J. H. Ye, *Chem. Commun.*, 2010, **46**, 1893.

159 D. E. Wang, H. F. Jiang, X. Zong, Q. A. Xu, Y. Ma, G. L. Li and C. Li, *Chem. – Eur. J.*, 2011, **17**, 1275–1282.

160 K. Wenderich, A. Klaassen, I. Siretanu, F. Mugele and G. Mul, *Angew. Chem., Int. Ed.*, 2014, **53**, 12476.

161 T. Tachikawa, T. Ochi and Y. Kobori, *ACS Catal.*, 2016, **6**, 2250.

162 S. Selcuk and A. Selloni, *Nat. Mater.*, 2016, **15**, 1107.

163 R. Li, H. Han, F. Zhang, D. Wang and C. Li, *Energy Environ. Sci.*, 2014, **7**, 1369.

164 J. Zhu, S. Pang, T. Dittrich, Y. Gao, W. Nie, J. Cui, R. Chen, H. An, F. Fan and C. Li, *Nano Lett.*, 2017, **17**, 6735.

165 S. Ida, A. Takashiba, S. Koga, H. Hagiwara and T. Ishihara, *J. Am. Chem. Soc.*, 2014, **136**, 1872.

166 A. L. Li, Z. L. Wang, H. Yin, S. Y. Wang, P. L. Yan, B. K. Huang, X. L. Wang, R. G. Li, X. Zong, H. X. Han and C. Li, *Chem. Sci.*, 2016, **7**, 6076.

167 P. L. Yan, X. Wang, X. J. Zheng, R. G. Li, J. F. Han, J. Y. Shi, A. L. Li, Y. Gan and C. Li, *Nano Energy*, 2015, **15**, 406.

168 D. O. Scanlon, C. W. Dunnill, J. Buckeridge, S. A. Shevlin, A. J. Logsdail, S. M. Woodley, C. R. A. Catlow, M. J. Powell, R. G. Palgrave, I. P. Parkin, G. W. Watson, T. W. Keal, P. Sherwood, A. Walsh and A. A. Sokol, *Nat. Mater.*, 2013, **12**, 798.

169 Y. Gao, J. Zhu, H. An, P. Yan, B. Huang, R. Chen, F. Fan and C. Li, *J. Phys. Chem. Lett.*, 2017, **8**, 1419.

170 V. Pfeifer, P. Erhart, S. Y. Li, K. Rachut, J. Morasch, J. Brotz, P. Reckers, T. Mayer, S. Ruhle, A. Zaban, I. M. Sero, J. Bisquert, W. Jaegermann and A. Klein, *J. Phys. Chem. Lett.*, 2013, **4**, 4182.

171 K. Maeda, *ACS Catal.*, 2013, **3**, 1486.

172 K. Sekizawa, K. Maeda, K. Domen, K. Koike and O. Ishitani, *J. Am. Chem. Soc.*, 2013, **135**, 4596.

173 H. Tada, T. Mitsui, T. Kiyonaga, T. Akita and K. Tanaka, *Nat. Mater.*, 2006, **5**, 782.

174 H. Li, Y. Gao, Y. Zhou, F. Fan, Q. Han, Q. Xu, X. Wang, M. Xiao, C. Li and Z. Zou, *Nano Lett.*, 2016, **16**, 5547.

175 J. N. Anker, W. P. Hall, O. Lyandres, N. C. Shah, J. Zhao and R. P. Van Duyne, *Nat. Mater.*, 2008, **7**, 442.

176 J. A. Schuller, E. S. Barnard, W. S. Cai, Y. C. Jun, J. S. White and M. L. Brongersma, *Nat. Mater.*, 2010, **9**, 193.

177 D. K. Gramotnev and S. I. Bozhevolnyi, *Nat. Photonics*, 2010, **4**, 83.

178 S. Linic, P. Christopher and D. B. Ingram, *Nat. Mater.*, 2011, **10**, 911.

179 C. Clavero, *Nat. Photonics*, 2014, **8**, 95.

180 S. Wang, Y. Gao, S. Miao, T. Liu, L. Mu, R. Li, F. Fan and C. Li, *J. Am. Chem. Soc.*, 2017, **139**, 11771.

181 M. G. Walter, E. L. Warren, J. R. McKone, S. W. Boettcher, Q. X. Mi, E. A. Santori and N. S. Lewis, *Chem. Rev.*, 2010, **110**, 6446.

182 M. G. Kibria, F. A. Chowdhury, S. Zhao, B. AlOtaibi, M. L. Trudeau, H. Guo and Z. Mi, *Nat. Commun.*, 2015, **6**, 6797.

183 D. Wang, T. Sheng, J. Chen, H.-F. Wang and P. Hu, *Nat. Catal.*, 2018, **1**, 291.

184 M. R. Nellist, F. A. L. Laskowski, J. Qiu, H. Hajibabaei, K. Sivula, T. W. Hamann and S. W. Boettcher, *Nat. Energy*, 2017, **3**, 46.

185 A. J. Bard, F. R. F. Fan, D. T. Pierce, P. R. Unwin, D. O. Wipf and F. M. Zhou, *Science*, 1991, **254**, 68.

186 A. J. Bard, *J. Am. Chem. Soc.*, 2010, **132**, 7559.

187 T. Kai, C. G. Zoski and A. J. Bard, *Chem. Commun.*, 2018, **54**, 1934.

188 L. Collins, M. Ahmadi, T. Wu, B. Hu, S. V. Kalinin and S. Jesse, *ACS Nano*, 2017, **11**, 8717.

189 J. Murawski, T. Graupner, P. Milde, R. Raupach, U. Zerweck-Trogisch and L. M. Eng, *J. Appl. Phys.*, 2015, **118**, 154302.

190 D. C. Coffey and D. S. Ginger, *Nat. Mater.*, 2006, **5**, 735.

191 R. Giridharagopal, G. E. Rayermann, G. Shao, D. T. Moore, O. G. Reid, A. F. Tillack, D. J. Masiello and D. S. Ginger, *Nano Lett.*, 2012, **12**, 893.

192 Z. Schumacher, Y. Miyahara, A. Spielhofer and P. Grutter, *Phys. Rev. Appl.*, 2016, **5**, 044018.

193 J. L. Garrett and J. N. Munday, *Nanotechnology*, 2016, **27**, 245705.